

Disordered hinge regions of the AP-3 adaptor complex promote vesicle budding from the late golgi in yeast

Mitchell Leih¹, Rachael L. Plemel², Matt West¹, Cortney G. Angers², Alexey J. Merz^{2,*}, and Greg Odorizzi^{1,*}

¹Department of Molecular, Cellular, and Developmental Biology, University of Colorado, Boulder, CO, USA

²Department of Biochemistry, University of Washington, Seattle, WA, USA

*Corresponding authors: odorizzi@colorado.edu, merza@uw.edu

Summary statement

The AP-3 adaptor in *Saccharomyces cerevisiae* has intrinsically disordered regions required for AP-3 vesicle budding from the Golgi. Without these hinges, AP-3 remains associated with Golgi compartments as they mature.

Keywords: adaptor, vesicle, Golgi, membrane, transport

ABSTRACT

Vesicles bud from maturing Golgi cisternae in a programmed sequence. Budding is mediated by adaptors that recruit cargoes and facilitate vesicle biogenesis. In *Saccharomyces cerevisiae*, the AP-3 adaptor complex directs cargoes from the Golgi to the lysosomal vacuole. The AP-3 core consists of small and medium subunits complexed with two non-identical large subunits, $\beta 3$ and δ . The C termini of $\beta 3$ and δ were thought to be flexible hinges linking the core to ear domains that bind accessory proteins involved in vesicular transport. We found by computational modeling that the yeast $\beta 3$ and δ hinges are intrinsically disordered and lack folded ear domains. When either hinge is truncated, AP-3 is recruited to the Golgi, but vesicle budding is impaired, and cargoes normally sorted into the AP-3 pathway are mistargeted. This budding deficiency causes AP-3 to accumulate on ring-like Golgi structures adjacent to GGA adaptors that, in wild-type cells, bud vesicles downstream of AP-3 during Golgi maturation. Thus, each of the disordered hinges of yeast AP-3 has a crucial role in mediating transport vesicle formation at the Golgi.

INTRODUCTION

Vesicle trafficking pathways ferry protein and lipid cargoes between different membrane-bound organelles in eukaryotic cells. This highly regulated process is orchestrated by cytosolic adaptor proteins specific to each trafficking pathway (reviewed in Robinson, 2015). Adaptor proteins capture and concentrate transmembrane proteins to be incorporated as cargoes of nascent transport vesicles. These adaptors also recruit other cytosolic proteins that facilitate vesicle budding and scission. In some cases, adaptors interact with proteins that mediate the fusion of vesicles with their target destination (reviewed in Angers and Merz, 2011). The diverse functions of vesicle adaptor proteins make them pivotal for maintaining cellular compartmentalization.

To accommodate the numerous different trafficking pathways within cells, a diversity of vesicle adaptors has evolved, including the family of Adaptor Protein (AP) complexes. Among the five characterized AP complexes, three (AP-1, AP-2, and AP-3) appear to be the most widespread throughout Eukarya (Hirst et al., 2011). Each AP complex functions in a distinct vesicle trafficking pathway. AP-2 is the best characterized AP complex and is well known for its function in endocytosis, while AP-1 functions in vesicular transport between endosomes and the Golgi (Robinson, 2015; Casler et al., 2021; Robinson et al., 2024). AP-3 is the least understood member among the conserved AP complexes, despite studies of AP-3 trafficking marking the advent of modern genetics (Morgan, 1910), and AP-3 deficiency resulting in various human pathologies (Horwitz et al., 2004; Dell'Angelica 2009; Bowman et al., 2019). AP-3 mediates vesicular transport to lysosomes and lysosome-related organelles. In mammalian cells, AP-3 vesicles bud from endosomal or Golgi compartments (Peden et al., 2004; Theos et al., 2005). In yeast, AP-3 vesicles bud from the Golgi (Cowles et al., 1997a; Stepp et al., 1997). However, yeast cells have a minimal endomembrane system in which the Golgi performs some endosomal sorting functions (Day et al., 2018), so the AP-3 pathway is likely homologous in these different cellular systems.

Each AP complex is a heterotetramer consisting of a small subunit, a medium subunit, and two large subunits that are non-identical but structurally similar. The quaternary structures of AP complexes are generally conserved: the N-terminal trunk domains of AP large subunits are compactly folded structures that assemble into heterotetramers with the medium and small subunits to form the complex core. The core binds lipids that are specific to membrane microdomains and also interacts with peptide sequences in the cytosolic domains of transmembrane protein cargoes (reviewed in Kirchhausen et al., 2014). The AP-1 and AP-3 cores also bind Arf GTPases that facilitate the membrane recruitment of each complex (Stamnes and Rothman, 1993; Traub et al., 1993; Seaman et al., 1996; Ooi et al., 1998; Drake et al., 2000; Begley et al., 2024 preprint).

The C terminus of each large subunit of mammalian AP-1 and AP-2 has a secondary structure known as an ear domain (also known as an appendage). Each ear connects to the core of the complex

through an intrinsically disordered “hinge” region consisting of 80-100 amino acids (Heuser and Keen, 1988). The AP-1 and AP-2 ears bind numerous accessory proteins that facilitate vesicle budding as well as other steps in the transport process (Owen et al., 1999; Traub et al., 1999; Praefcke et al., 2004; Ritter et al., 2004; Schmid et al., 2006; reviewed in Kirchhausen et al., 2014). Based on its functional homology, AP-3 is anticipated to interact similarly with accessory proteins via C-terminal ear domains that are linked by disordered hinge regions to one or both large subunits of the complex. Indeed, a handful of proteins that facilitate vesicular transport are known to bind the C-terminal regions of large subunits in AP-3, including Vps41, a member of the HOPS protein complex that tethers AP-3 vesicles at the target vacuole/lysosome membrane (Rehling et al., 1999; Angers and Merz, 2009; Cabrera et al., 2010; Asensio et al., 2013; Schoppe 2020). However, in reconstructions of yeast and human AP-3 imaged by cryo-electron microscopy (cryo-EM), the C termini of the large subunits were not resolved (Schoppe et al., 2021; Begley et al., 2024 preprint), so the extent of structural conservation in these regions of AP-3 is unknown.

Here we present computational modeling suggesting that a folded ear domain is not present at the C terminus of either large subunit of yeast AP-3. Instead, each C-terminal region is predicted to be entirely disordered. We investigated the role of each disordered hinge in yeast AP-3 by testing the effect of truncating each region. Our results show that neither hinge truncation disrupts the recruitment of AP-3 complexes to membranes, but each hinge is required for AP-3 vesicle budding from the Golgi. The consequences of AP-3 budding deficiency include Golgi enlargement and aberrant colocalization of AP-3 with GGA adaptors that normally function downstream of AP-3 during Golgi maturation, though GGA remains functional under these abnormal conditions.

RESULTS

Ear domain structures are absent from yeast AP-3 complexes in computational models

Cryo-EM analysis had shown that the yeast AP-3 core has a structure similar to the mammalian AP-1 and AP-2 core structures, although variations in flexibility were apparent between the complexes (Schoppe et al., 2021). Absent from the AP-3 structure was the C-terminal region of each large subunit, Apl5 and Apl6 (the δ and β 3 subunits, respectively), suggesting each region is disordered and does not contribute to quaternary structure. Because of the overall structural and functional conservation among AP complexes, the C terminus of each yeast AP-3 large subunit was expected to emanate from the core as an unstructured stretch of amino acids, with at least one of these regions linking to a folded ear domain (Edeling et al., 2006). However, computational modeling by AlphaFold2 (Fig. 1A) and Metapredict (Fig. S1A) indicate that the C-terminal regions of Apl5 and Apl6 lack ear domains and are, instead, mostly disordered, with no tertiary structure and only short

regions of predicted α -helical secondary structure. To maintain consistency with nomenclature used for other AP complexes, the intrinsically disordered C-terminal regions of Apl5 and Apl6 are referred to here as hinges, though they do not appear to link the AP-3 core to folded ear domains as they do in AP-1 and AP-2.

Unlike yeast AP-3, the human AP-3 δ subunit and each of the two human β 3 subunit isoforms (β 3A and β 3B) are predicted by AlphaFold2 to have folded ear domains at the C termini of their disordered hinges (Fig. 1B). The absence of ear domains in yeast δ and β 3 raised the possibility that this secondary structure did not evolve in any of the AP complexes in *S. cerevisiae*. However, in contrast to AP-3, AlphaFold2 does predict a folded ear domain at the C terminus of the yeast AP-1 γ subunit (Apl4) and AP-2 α subunit (Apl3), while ear domains are absent in β subunits of yeast AP-1 and AP-2 (Fig. S1B). Fig. 1C shows revised models comparing the AP-1, AP-2, and AP-3 complexes in *S. cerevisiae* and humans, based on the available crystallographic data and our computational modeling.

AP-3 in mammalian cells can function independently of clathrin (Zlatic et al., 2013), although direct binding of clathrin heavy chain to the human β 3A subunit was detected *in vitro* (Dell'Angelica et al., 1998). This interaction depends on an amino acid sequence in the hinge of β 3A that matches a conserved clathrin-binding motif (CBM; Dell'Angelica, 2001). The CBM consensus sequence (L Φ [polar] Φ [D/E]) is absent from Apl5 and Apl6 in yeast AP-3, although the Apl5 hinge has a CBM-like sequence (LLDLN) that lacks the negatively charged amino acid at position 5. We observed that clathrin in yeast lysates was unable to bind the purified hinge regions of either Apl5 or Apl6 *in vitro*, whereas clathrin binding to the hinge of the AP-1 γ subunit (Apl4) was readily detected (Fig. 1D). This result agrees with prior work indicating that, in *S. cerevisiae*, clathrin does not bind AP-3 (Yeung et al., 1999), and AP-3 trafficking is unaffected by genetic mutation of clathrin (Vowels and Payne, 1998; Schoppe et al., 2020). Additionally, we found that deletion of the *APL5* or *APL6* genes did not exacerbate the growth defect of cells bearing the *chc1-521* mutation in clathrin heavy chain, unlike deletion of AP-1 genes in *chc1-521* mutant cells (Fig. S1C), which is also consistent with yeast AP-3 functioning independently of clathrin (Yeung et al., 1999).

AP-3 trafficking in yeast requires the disordered hinge regions

AP-3 mediates vesicular transport from the Golgi to the vacuole in yeast (Fig. 2A; Cowles et al., 1997a; Stepp et al., 1998). We investigated the extent to which this pathway requires the δ or β 3 hinges by progressively truncating the C terminus of Apl5 versus Apl6 (Fig. S2A). The effects of these truncations on AP-3 trafficking were evaluated using GNSS, a synthetic transmembrane protein cargo that serves as a qualitative and quantitative reporter of AP-3 sorting efficiency (Fig. 2A). GNSS is

almost identical to GNSI, a synthetic AP-3 cargo we previously characterized (Plemel et al., 2021). Both GNSS and GNSI have green fluorescent protein (GFP) fused to the cytoplasmic domain of the v/R-SNARE, Nyv1, which has a sorting signal that mediates entry into AP-3 vesicles budding from the Golgi (Reggiori et al., 2000). The transmembrane domain of GNSS/GNSI is derived from the v/R-SNARE, Snc1, while the luminal/exoplasmic domain of GNSS has two copies of the invertase enzyme encoded by the *SUC2* gene (Fig. 2A), whereas GNSI has one copy of invertase (Plemel et al., 2021). In wild-type cells, GNSS and GNSI are sorted from the Golgi to the vacuole membrane via the AP-3 pathway, but in mutant cells lacking AP-3 function, these reporters are re-routed into the secretory pathway and delivered to the plasma membrane (Reggiori et al., 2000; Plemel et al., 2021).

Using a chromogenic assay that detects invertase activity at the cell surface (Darsow et al., 2000; Plemel et al., 2021), we observed mistargeting of GNSS to the plasma membrane in mutant strains lacking either Apl5 (*apl5* Δ) or Apl6 (*apl6* Δ) but not in wild-type yeast or in *apl5* Δ or *apl6* Δ cells harboring plasmids encoding the wild-type *APL5* or *APL6* gene (Fig. S2B). Deletion-mutant strains transformed with the series of plasmid-borne *apl5* or *apl6* truncation alleles showed partial to complete loss of GNSS sorting (Fig. S2B). We further analyzed *apl5-710* Δ and *apl6-743* Δ truncation-mutant alleles because of their effects on AP-3 localization, as described below. The extent to which *apl5-710* Δ and *apl6-743* Δ caused rerouting of the GNSS cargo into the secretory pathway was quantified by measuring the fraction of total cellular invertase activity at the plasma membrane of cells grown in liquid culture. We found that ~80% of GNSS is missorted in *apl5-710* Δ cells, while ~50% of this AP-3 cargo is missorted in *apl6-743* Δ cells (Fig. 2B). These values are consistent with our microscopic analyses, which show increased GNSS fluorescence at the plasma membrane of *apl5-710* Δ cells compared to *apl6-743* Δ cells, whereas in wild-type cells, virtually all of the GNSS fluorescence is at the vacuole membrane (Fig. 2C). Thus, efficient cargo trafficking via the AP-3 pathway depends on the disordered hinges of the two AP-3 large subunits.

Truncation of either hinge region causes AP-3 accumulation at the Golgi

Having established that yeast AP-3 cargo sorting is disrupted by truncating the disordered hinge region of either the AP-3 β 3 (Apl6) or δ (Apl5) subunits, we investigated the effects of these truncations on the intracellular localization of the AP-3 complex. We constructed *APL5-GFP* and *APL6-GFP* fusions that were chromosomally integrated and fully functional, based on GNSS sorting assays (Fig. S3A). In wild-type cells, these GFP fusions were previously shown to localize in close proximity to Sec7 (Day et al., 2018). Sec7 is a marker of the TGN (e.g., Daboussi et al., 2012; Day et al., 2018; Franzusoff et al., 1991), where it functions as a guanine nucleotide exchange factor for the redundant Arf1 and Arf2 GTPases in *S. cerevisiae* (Sata et al., 1998; Losev et al., 2006; Casanova, 2007). Using confocal fluorescence microscopy, we examined the localization of Apl5-GFP or Apl6-GFP relative to Sec7

fused to the MARS red fluorescent protein in yeast expressing wild-type or truncated *apl6* or *apl5* alleles (unpublished observations). In this analysis, we found that the *apl6-743Δ* and *apl5-710Δ* truncations caused AP-3 (labeled by Apl5-GFP or Apl6-GFP, respectively) to accumulate at enlarged structures that were round and sometimes hollow, reminiscent of rings or donuts. For this reason, we focused our studies on understanding the effects of these specific truncation-mutant alleles.

In wild-type cells observed by conventional confocal fluorescence microscopy, we found numerous Apl5-GFP puncta, many of which were in close proximity to puncta labeled by Sec7-MARS (Fig. 3A). We scored ~45% of Sec7-MARS compartments as colocalizing with either Apl5-GFP or Apl6-GFP (Fig. 3B). Our observation that <50% of Sec7-MARS colocalizes with AP-3 agrees with work showing that AP-3 is recruited to maturing Golgi cisternae upstream of Sec7 (Day et al., 2018; Tojima et al., 2019; Highland and Fromme, 2021). In *apl6-743Δ* cells, we observed Apl5-GFP puncta that were substantially enlarged compared to Apl5-GFP puncta in wild-type *APL6* cells (Fig. 3A). Moreover, the fraction of Sec7-MARS overlapping Apl5-GFP almost doubled in response to Apl6 truncation (Fig. 3B). We observed a similar localization pattern for Apl6-GFP: ~40% of Sec7-MARS puncta colocalized with Apl6-GFP in wild-type *APL5* cells, while in *apl5-710Δ* cells, Apl6-GFP puncta were enlarged (Fig. S3B), and the percentage of overlapping Sec7-MARS puncta increased more than two-fold (Fig. 3B). Therefore, truncation of the hinge region of either AP-3 large subunit causes the AP-3 complex to accumulate at TGN compartments marked by Sec7. A plausible interpretation of these findings is that the hinge regions are needed for successful completion of AP-3 budding from the Golgi, but not for AP-3 recruitment to Golgi membranes. As expected, Apl5-GFP puncta were not seen in *apl6Δ* cells (Fig. 3A), and Apl6-GFP puncta were not observed in *apl5Δ* cells (Fig. S3B). Moreover, neither of these GFP fusions was localized to puncta in deletion-mutant strains lacking either the *APM3* or *APS3* gene that encodes the medium or small AP-3 subunit, respectively (unpublished results). All four subunits, therefore, are required for efficient recruitment of AP-3 complexes to the Golgi.

In the above analyses, we occasionally observed Apl5-GFP or Apl6-GFP in a circular, donut-shaped pattern surrounding Sec7-MARS, but only in mutant cells bearing a hinge truncation, not in cells expressing full-length Apl6 and Apl5 (arrowheads in Fig. 3A and Fig. S3B). Using a spinning disk confocal microscope equipped for super-resolution imaging, puncta of GFP-tagged AP-3 surrounding Sec7-MARS were more clearly evident and appeared as segmented radial structures with interspersed microdomains of AP-3 (arrowheads in Fig. 3C and in Fig. S3C). Additionally, Sec7-positive structures were more clearly resolved by super-resolution imaging than they were in our conventional confocal fluorescence images (Fig. 3A) and showed a range of morphologies, with the majority seen as oblong cisterna-like structures and a minority observed as crescents or fully rounded structures (Fig. S3D). Clusters of AP-3 with Sec7 were present in >90% of *apl6-743Δ* and *apl5-710Δ* mutant cells but were rarely observed (~5%) in wild-type cells expressing full-length AP-3 subunits

(Fig. 3C; $n \geq 200$). The sharp increase in clusters of AP-3/Sec7 fluorescence again indicates that AP-3 aberrantly accumulates on TGN compartments when the disordered hinge of either AP-3 large subunit is truncated.

Sec7 is one of three GEFs that act in a spatiotemporal sequence to activate the Arf1 and Arf2 GTPases during Golgi maturation. Upstream of Sec7 at the TGN, Arf1/Arf2 activation is catalyzed by Gea1 at the early Golgi, followed by Gea2 at the medial and late Golgi (Peyroche et al., 1996; Spang et al., 2001; Gustafson and Fromme, 2017). Activated (GTP-bound) Arf1/Arf2 recruit diverse proteins, including vesicle adaptors (Goldberg, 1999; Hirst et al., 2000; Boman et al., 2000; Dell'Angelica et al., 2000; Puertollano et al., 2001). Sequential activation of Arf1/Arf2, in combination with other signals, is thought to result in waves of vesicle budding from Golgi compartments as they mature from cis- to medial- to late-Golgi and the TGN (Bui et al., 2009; Highland and Fromme, 2021).

To determine if AP-3 hinge truncations affect AP-3 recruitment to Golgi compartments upstream of Sec7, we examined the localization of Apl5-GFP or Apl6-GFP in cells expressing a Gea2-MARS fusion protein. In wild-type cells, we observed Gea2-MARS colocalizing with GFP-tagged AP-3 subunits at a frequency similar to Sec7-MARS colocalization with AP-3. However, Gea2-MARS colocalization with AP-3 was modestly decreased in cells expressing AP-3 hinge truncations (Fig. 3D,E). Together with the increase in AP-3 and Sec7-MARS colocalization that we observed in AP-3 hinge truncation mutants (Fig. 3B), this result suggests hinge truncations cause aberrant retention of AP-3 at Golgi compartments undergoing medial- to late-Golgi/TGN maturation. Notably, a range of Gea2-MARS localization patterns was observed in AP-3 hinge truncation mutants compared to wild-type cells. Among the patterns of Gea2-MARS localization seen in hinge truncation mutants were donuts that were directly adjacent to Apl5-GFP or Apl6-GFP donuts, indicating that, when AP-3 vesicle budding is blocked, AP-3 accumulates at membranes distinct from compartments containing Gea2 (arrowheads in Fig. 3D and Fig. S3E,F).

Hinge truncations inhibit AP-3 vesicle budding

Based on the shift of AP-3 toward Sec7-marked TGN compartments in mutant cells expressing AP-3 hinge truncations, we further examined the spatial relationship between AP-3 and Sec7 by high-speed time-lapse microscopy. Samples were illuminated using variable angle epifluorescence (VAEF) microscopy to decrease photodamage (Konopka and Bednarek, 2008), and fluorescence emission signals were split so that paired images of GFP-tagged AP-3 and Sec7-MARS could be captured simultaneously. Analyses of 30-second movies acquired at 20 frames per second revealed two populations of Apl5-GFP puncta in wild-type *APL6* cells. The first set consisted of puncta that were

relatively static and often colocalized with Sec7-MARS; the second set consisted of Apl5-GFP puncta that were extremely dynamic, moving away and sometimes toward the more static population of Apl5-GFP/Sec7-MARS puncta (see Movie 1). In marked contrast to wild-type *APL6* cells, the dynamic population of Apl5-GFP puncta was largely or completely missing in *apl6-743Δ* cells; instead, almost all Apl5-GFP puncta exhibited constrained movement when paired with the *apl6-743Δ* mutation, often orbiting Sec7-MARS, rather than moving away (see Movie 2). The relatively immobile population of Apl5-GFP and Sec7-MARS puncta corresponds to the clusters of AP-3 and Sec7 in 3-D image stacks that we observed by confocal microscopy at much lower frame rates (Fig. 3A,C).

Tracking individual particles in 30-second movies demonstrated the dramatic difference in the mobility of Apl5-GFP in wild-type *APL6* versus *apl6-743Δ* mutant cells. Examples are shown for single cells in Fig. 4A,B. Particle displacements are quantitated from cell populations in Fig. 4C,D. A similar pattern of movement was observed for Apl6-GFP, which exhibited high mobility in wild-type *APL5* cells but showed restricted movement in *apl5-710Δ* mutant cells (Fig. 4B,D; see Movies 3 and 4). The restricted mobility of AP-3 puncta and accumulation of AP-3 at Sec7-positive Golgi resulting from AP-3 hinge truncations suggests that AP-3 vesicle budding from the Golgi requires the disordered hinge of each large subunit. We infer that the slow-moving AP-3 puncta in wild-type cells are incipient vesicles forming at the Golgi, while the fast-moving puncta are free, post-Golgi AP-3 vesicles that have not yet docked at the vacuole target membrane. The loss of fast-moving AP-3 puncta and retention of AP-3 at Sec7-positive Golgi in hinge truncation mutants support working models in which each AP-3 hinge is needed for vesicle budding. This interpretation is buttressed by previous work showing that AP-3 does not rapidly uncoat upon budding. Instead, AP-3 remains associated with the transport vesicle until the vesicle has docked or fused at the vacuole membrane (Angers and Merz, 2011; Schwartz et al., 2017; Schoppe et al., 2020).

Based on the changes observed in Gea2 and Sec7 localization resulting from AP-3 hinge truncations (Fig. 3), we investigated the localization of these Arf GEFs relative to each other by super-resolution microscopy. In wild-type cells, Gea2-mNeon and Sec7-MARS rarely overlap (Fig. 5A,B), consistent with previous observations indicating that Golgi compartments are sequentially marked by each GEF (Bui et al., 2009; Highland and Fromme, 2021). When either hinge of AP-3 is truncated, spatial separation between Gea2-mNeon and Sec7-MARS is maintained (Fig. 5B,C), but each exhibits radial patterning. This patterning was unlike the punctate or tubular shapes observed in wild-type cells, but similar to what was observed for each GEF when coexpressed with GFP-tagged AP-3 in *apl6* or *apl5* truncation-mutant cells (Fig. 3). Despite their radial distributions, no substantial differences were seen in the size or number of Gea2-mNeon or Sec7-MARS puncta in truncation-mutant cells compared to wild-type cells. However, there was a slight difference in *apl5Δ* cells, which had larger puncta of Sec7-MARS that likely represent donuts whose centers were not resolved by light microscopy (Fig. S4A-D).

The changes in the localization patterns of Gea2 and Sec7 prompted us to investigate if AP-3 hinge truncations altered Golgi morphology, which we examined at higher resolution using electron tomography. In tomographic reconstructions of wild-type *S. cerevisiae*, Golgi cisternae appear as elongated, fenestrated flat disk-shaped compartments or as curved/rounded compartments (Fig. 5D,E; see Movie 5). When measuring the total surface area of these Golgi membranes in wild-type cells, flat Golgi are consistently larger than their rounded counterparts (Fig. S4E,F). The membrane surface areas of flat Golgi remain consistent when AP-3 hinges are truncated or when AP-3 large subunits are deleted (Fig. S4E,F). AP-3 large-subunit deletions and hinge truncations caused some rounded Golgi to more than double their total membrane surface areas, though this effect was not statistically significant (Fig. S4E,F; see Movie 5 and Movie 6). Immunogold labeling of thin sections indicated that Apl5-GFP and Apl6-GFP localize to both flat and rounded compartments in wild-type cells. In contrast, AP-3 hinge truncations resulted in twice as much immunogold labeling on rounded Golgi relative to flat Golgi (Fig. S4G-J), suggesting that unbudded AP-3 complexes might prefer curved Golgi membranes, though more direct experimentation will be needed to determine the extent to which AP-3 has this property.

Budding-defective AP-3 commingles with downstream Golgi vesicle adaptors

Studies of the temporal and spatial dynamics of transport vesicle adaptors in yeast indicate that AP-3 is recruited to the Golgi prior to two other adaptors, GGA and AP-1. GGA adaptors (Gga1 and Gga2) mediate vesicular transport from the TGN to late endosomes (Black and Pelham, 2000; Dell'Angelica et al., 2000; Hirst et al., 2000; Zhdankina et al., 2001); AP-1 mediates recycling from TGN/early endosomal compartments to earlier Golgi cisternae (Daboussi et al., 2012; Day et al., 2018; Casler et al., 2019). GGA recruitment to the TGN coincides with Sec7 arrival, both spatially and temporally, and precedes AP-1 recruitment to Sec7-positive compartments (Daboussi et al., 2012; Day et al., 2018; Casler et al., 2020; Tojima et al., 2019). Further supporting this spatiotemporal sequence, genetic studies had shown that sorting into the AP-3 pathway occurs upstream of GGA sorting (Cowles et al., 1997b). Because AP-3 hinge truncations cause accumulation of AP-3 at Sec7 compartments (Fig. 3), we investigated the extent to which hinge truncations affect the localization of AP-3 relative to GGA and AP-1.

In wild-type cells, mCherry-tagged GGA (Gga2-mCh) was frequently observed as clusters of puncta arranged in a circular array (Fig. S5A). These radial arrangements resembled the donut-shaped clusters of AP-3 puncta in cells in which Apl5 or Apl6 had been truncated (Figs 3,4,S3,S4). By super-resolution microscopy, an individual Apl5-GFP punctum was seen occasionally inserted between the radial Gga2-mCh puncta, but the majority of Apl5-GFP puncta were spatially separated from Gga2-mCh in wild-type cells (Fig. 6A). In *apl6-743Δ* cells, however, puncta marked by Gga2-mCh versus

Apl5-GFP were frequently seen alternating in ring-like structures but with little direct overlap (Fig. 6B, upper panel; Fig. 6C,D). Similar spatial relationships between Apl6-GFP and Gga2-mCh were seen in wild-type *APL5* versus mutant *apl5-710Δ* cells (Fig. S5A,B). Taken together, these results indicate that budding-deficient AP-3 complexes accumulate and are retained on Golgi compartments to which Gga2 is recruited, but each adaptor preferentially occupies distinct sub-micron membrane domains.

Unlike Gga2-mCh, AP-1 (labeled by Apl4-mCh) was predominantly observed in wild-type *APL6* cells as unorganized clusters or distinct puncta that were more spatially separated from Apl5-GFP puncta (Fig. 6E). Concurrently, the extent of overlap between Apl4-mCh and Apl5-GFP is considerably less than the overlap observed between Apl5-GFP and Gga2-mCh (Fig. 6F). In *apl6-743Δ* cells, Apl4-mCh puncta remained mostly separate from the radial clusters of Apl5-GFP puncta (Fig. 6E, lower panel; Fig. 6F), though the frequency of overlap doubled, and Apl4mCh puncta were occasionally seen intertwined with Apl5-GFP puncta (arrowheads in Fig. 6E). A similar pattern was observed in wild-type *APL5* versus *apl5-710Δ* cells expressing Apl6-GFP with Apl4-mCh (Fig. 5F; Fig. S5C). Collectively, these observations indicate that the AP-3 budding defect caused by hinge truncations results in AP-3 retention at late Golgi/TGN compartments as they mature, with AP-3 accumulating predominantly alongside GGA adaptors and some fraction of AP-3 persisting at the Golgi until AP-1 is recruited.

AP-3 dysfunction does not prevent GGA sorting activity

The data described above indicate that budding-defective AP-3 persists at Golgi cisternae as these compartments mature and acquire GGA and AP-1 vesicle adaptors, which normally operate downstream of AP-3. Under these conditions, AP-3 aberrantly colocalizes most strongly with Gga2, which (with its redundant paralog, Gga1) functions to sort transmembrane proteins into the VPS pathway to deliver cargoes to prevacuolar endosomes en route to the vacuole. The best characterized cargo of the VPS pathway is Vps10, a transmembrane receptor for the soluble vacuolar hydrolase, carboxypeptidase Y (CPY; Marcusson et al., 1994). After binding newly synthesized CPY in the Golgi, Vps10 is sorted by Gga1/Gga2 into vesicles that bud from the TGN and fuse with the prevacuolar endosome, where Vps10 releases CPY and is subsequently retrieved to the Golgi through the retromer pathway (Seaman et al., 1998).

Deletion of AP-3 subunit genes does not affect CPY sorting (Cowles et al., 1997a; Stepp et al., 1997). Likewise, genetic disruption of the VPS pathway does not affect the sorting of AP-3 cargoes (Cowles et al., 1997b). Thus, the AP-3 and VPS pathways have been considered to be mechanistically distinct. However, because of the abnormal retention of budding-defective AP-3 at Golgi

compartments to which GGA adaptors are recruited (Fig. 6C), we investigated whether GGA function is affected by the AP-3 hinge truncations. For this analysis we used the CPY-invertase fusion protein that has been used extensively to study the VPS pathway (Bankaitis et al., 1986). As in our analyses of GNSS sorting (Fig. S2A), we evaluated CPY-invertase sorting in cells growing on agar medium using the chromogenic assay that detects secreted invertase activity (Darsow et al., 2000). Wild-type cells efficiently sort CPY-invertase to the vacuole and, thus, colonies appear white in this assay, but mutations that disrupt Vps10 trafficking between the TGN and prevacuolar endosome (e.g., *vps4Δ*) cause aberrant secretion of newly synthesized CPY-invertase, resulting in darkened colonies (Fig. 7A,B). CPY-invertase secretion was minimal upon deletion of *APL5* or *APL6*, consistent with earlier work (Cowles et al., 1997a; Stepp et al., 1997). Similarly, no defect in CPY sorting was detected in *apl5-710Δ* or *apl6-743Δ* cells (Fig. 7A,B). Thus, the aberrant retention of AP-3 at Golgi compartments does not impede GGA-mediated sorting (Fig. 7C).

DISCUSSION

Prior studies have shown that the C termini of mammalian AP-1 and AP-2 large subunits consist of unstructured amino acid sequences that act as hinges linking the core of each complex to ear domain secondary structures. Ear domains bind diverse accessory proteins that facilitate different stages of vesicular transport (reviewed in Kirchhausen et al., 2014; Robinson, 2015). Because of their central role in AP-1 and AP-2 function, we were surprised to find that computational analyses predicted neither the $\beta 3$ subunit (Apl6) nor the δ subunit (Apl5) of yeast AP-3 has an ear domain, though both subunits are predicted to have hinges that are mostly disordered, similar to those observed for AP-1 and AP-2 hinges. Phylogenetic studies have also suggested that ear domains are absent from β subunits in the AP-1, AP-2, and AP-3 complexes in the majority of fungal species (Martzoukou et al., 2017). Nonetheless, ear domains appear to have evolved in *S. cerevisiae* (and potentially in other fungi), based on computational models predicting an ear domain near the C-terminal end of an unstructured hinge in the γ subunit of AP-1 (Apl4) and the α subunit of AP-2 (Apl3). Why ear domains are not uniformly present in AP complexes is unclear.

Despite lacking folded ear domains, our experiments show that the hinges of Apl6 ($\beta 3$) and Apl5 (δ) are required for AP-3 function in yeast. Truncation of either hinge disrupts cargo trafficking from the Golgi to the vacuole via the AP-3 pathway while having no apparent effect on AP-3 complex assembly, based on mass spectrometry of immuno-isolated AP-3 complexes expressed from yeast cells expressing truncated subunits (unpublished results). Hinge truncations also do not disrupt recruitment of AP-3 to the Golgi (Fig. 3). Instead, each truncation inhibits AP-3 vesicle budding, resulting in the accumulation of AP-3 at or near TGN compartments marked by Sec7. We found no evidence that unbudded AP-3 complexes trap cargoes at the Golgi, as neither the *apl6-743Δ* truncation

nor the *apl5-710Δ* truncation caused GNSS cargo fluorescence to accumulate at intracellular puncta (Fig. 2). Likewise, the *apl6-743Δ* truncation did not enhance the recovery of cargoes with immunoprecipitated AP-3 complexes that were analyzed by mass spectrometry or by western blot (unpublished results), though we cannot rule out the possibility that cargo accumulations might be detected using other methods. Like truncation of the yeast AP-3 δ or $\beta 3$ subunits, C-terminal truncation of the mouse $\beta 3A$ subunit was found to disable AP-3 function but not its recruitment to perinuclear (Golgi/endosomal) compartments in cultured cells (Peden et al., 2002), though this earlier study did not directly determine whether mouse $\beta 3A$ truncation affected the budding of AP-3 vesicles. Curiously, cargo endocytosis in HeLa cells was unaffected by truncation of the AP-2 $\alpha 2$ subunit or by mutations in accessory-binding sites that had been identified in this subunit (Motley et al., 2006), though $\alpha 2$ truncation altered the kinetics of endocytic vesicle formation and disrupted events downstream of vesicle budding (Aguet et al., 2013; Reis et al., 2015).

Our observation that truncating either AP-3 hinge disables AP-3 vesicle budding was most vividly revealed by high-speed time-lapse fluorescence microscopy, which showed truncated AP-3 is relatively immobile compared to wild-type AP-3. This disparity in motion raises the possibility that the unstructured hinges of AP-3 have a direct role in membrane remodeling and fission, as has been observed in other proteins with intrinsically disordered regions (Snead et al., 2018). Another possibility is that the biophysical properties of the disordered hinges control the mobility and/or orientation of AP-3 complexes at the membrane surface, as has been seen for the disordered N terminus of oxysterol-binding protein at membrane contact sites between the endoplasmic reticulum and the TGN (Jamecna et al., 2019). These hypotheses are not mutually exclusive with one another or with the possibility that the hinges of *Apl5* and *Apl6* might recruit other proteins that facilitate AP-3 vesicle budding, as observed for other AP complexes (Kirchhausen et al., 2014). For example, the hinges of AP-1 and AP-2 large subunits interact with clathrin coat proteins. In the case of yeast AP-3, however, clathrin is an unlikely partner because cargo sorting via the AP-3 pathway in *S. cerevisiae* is unaffected by mutation of the clathrin heavy or light chain genes (Vowels and Payne, 1998; Schoppe et al., 2020). Clathrin function is also dispensable for AP-3 vesicle budding in cultured rat cells (Zlatic et al., 2013), and AP-3 subunits do not copurify with clathrin-coated vesicles isolated from bovine brain (Newman et al., 1995; Simpson et al., 1996; Dell'Angelica et al., 1997). The ability of AP-3 to operate independently of clathrin might be explained by phylogenetic analyses suggesting that AP-3 is the most ancient member of the AP family (Hirst et al., 2011).

Understanding the mechanisms of AP-3 function would benefit from the identification of accessory proteins that interact with the hinges of the $\beta 3$ and δ subunits. Such interaction partners are expected to include factors that facilitate multiple steps in AP-3 vesicle trafficking, like many of the proteins that interact with the hinge or ear domains of AP-1 and AP-2 large subunits (Kirchhausen et al., 2014). While relatively few AP-3 binding partners have been identified thus far, a well-

characterized interactor is Vps41, which binds the hinge of Apl5 in yeast (Rehling et al., 1999). Vps41 interaction with AP-3 is conserved in mammalian cells (Salazar et al., 2009), and earlier studies speculated that Vps41 replaces clathrin as an outer-shell coat protein for AP-3 vesicles (Rehling et al., 1999; Darsow et al., 2001; Asensio et al., 2013). However, Vps41 was subsequently characterized as a subunit of the homotypic fusion and vacuole protein sorting (HOPS) membrane tethering complex (Seals et al., 2000), and later studies established that it is in the context of HOPS in which Vps41 interacts with Apl5, serving to capture AP-3 vesicles at the vacuole/lysosome rather than facilitate AP-3 vesicle budding (Angers and Merz, 2009; Schoppe et al., 2020).

The Vps41 binding site in AP-3 is located in the hinge sequence that was deleted in *apl5-710Δ*. Though our results clearly show Apl5 truncation inhibits AP-3 vesicle budding from the Golgi, defective AP-3 cargo sorting also occurs upon genetic disruption of membrane fusion at the vacuole (Schwartz et al., 2017; Plemel et al., 2021). This fusion step relies on HOPS-mediated tethering of AP-3 vesicles to the vacuole membrane (Angers and Merz, 2009). The defect in AP-3 vesicle budding combined with the loss of Vps41 binding to AP-3 in *apl5-710Δ* cells could explain why this mutant strain has a stronger cargo-missorting phenotype (~80% missorted GNSS) compared to *apl6-743Δ* cells (~50% missorted GNSS), though testing this hypothesis would require creative restoration of the Vps41 binding site in cells expressing the truncated Apl5 protein. In either case, the different severity to which truncation of Apl5 versus Apl6 affects AP-3 cargo sorting suggests that the hinge regions are not functionally redundant, even though truncation of either hinge impairs the budding of AP-3 vesicles. We anticipate that the Apl5 and Apl6 hinges bind distinct accessory proteins involved in AP-3 vesicle trafficking, though some interaction partners might be shared, as has been observed for hinge-ear regions of other AP complexes (Traub, 2005).

A search for regulators of AP-3 vesicle trafficking in yeast was carried out by proximity-dependent biotinylation using Apl5 fused at its C terminus to a biotin ligase (Schoppe et al., 2020). This approach resulted in the identification of Age2, one of several GTPase accelerating proteins (GAPs) that function to inactivate Arf GTPases (Poon et al., 2001). In their active GTP-bound state, Arfs associate with Golgi membranes and facilitate the recruitment of AP-3 (Ooi et al., 1998; Drake et al., 2000) and other Golgi vesicle adaptors (reviewed in D'Souza-Schorey and Chavrier, 2006). In *S. cerevisiae*, the redundant Arf1 and Arf2 GTPases are activated by three distinct GEFs operating sequentially as Golgi cisternae mature. Gea1 functions at early Golgi cisternae, while Gea2 associates with medial/trans-Golgi compartments, and Sec7 localizes to the TGN (Bui et al., 2009; Highland and Fromme, 2021). The distribution of these GEFs can, therefore, serve to identify the maturation state of individual Golgi compartments. In static images obtained by confocal fluorescence microscopy, we observed that AP-3 in wild-type cells is more strongly colocalized with Gea2 than with Sec7. However, AP-3 shifts away from Gea2 toward Sec7 when AP-3 vesicle budding is impaired. These results suggest AP-3 recruitment begins at medial/late-Golgi compartments and continues as these

compartments mature into the TGN. This inference is in line with time-lapse imaging studies tracking the arrival and departure of different adaptors relative to Sec7, which established an order of vesicle budding during the maturation of late Golgi compartments: AP-3 is the first adaptor recruited in this sequence and peaks in abundance as Sec7 arrives, while GGA recruitment coincides with Sec7 and is followed by AP-1 (Daboussi et al., 2012; Day et al., 2018; Tojima et al., 2019; Casler and Glick, 2020; Fromme and Highland, 2021).

Using super-resolution confocal fluorescence microscopy, we resolved the positional relationships between AP-3, GGA, and AP-1 in more detail. In wild-type cells, Gga2 puncta were frequently seen in a radial pattern that was occasionally infiltrated by AP-3 puncta. In contrast, AP-3 budding-deficiency caused Gga2 and AP-3 puncta to extensively commingle but remain distinct from one another, alternating in a donut-shaped pattern. The circular distribution of Gga2 and AP-3 puncta correlates with our EM studies, which showed accumulation of AP-3 large subunits on rounded Golgi by immunolabeling. At the circular structures imaged by super-resolution confocal fluorescence microscopy, the alternating pattern of Gga2 and AP-3 puncta is consistent with these Golgi adaptors localizing to discrete membrane microdomains. This partitioning might explain why GGA sorting activity remains unperturbed in AP-3 budding-deficient cells despite the neighboring accumulation of AP-3. In wild-type cells, AP-3 and AP-1 puncta rarely overlapped with one another, but, as with GGA, AP-1 colocalization with AP-3 doubled in AP-3 budding-defective cells. Thus, unbudded AP-3 remains associated with Golgi compartments as late as AP-1 recruitment, which peaks downstream of GGA recruitment during Golgi maturation (Daboussi et al., 2012; Day et al., 2018; Tojima et al., 2019; Highland and Fromme, 2021).

The hinge truncations that disable AP-3 budding also caused a shift in the localization patterns of Gga2 and Sec7. Each of these GEFs exhibit punctate or tubular distributions in wild-type cells, but both adopted a more rounded pattern of fluorescence in cells bearing AP-3 hinge truncations, much like we observed for AP-3 itself under these conditions. Again, this shape change correlated with the accumulation of round Golgi compartments in truncation-mutant cells, as observed by electron tomography, which was also seen in *apl5Δ* and *apl6Δ* deletion-mutant cells. Why Golgi structure might be impacted by AP-3 dysfunction has not been determined, though it would seem likely to result from the continued presence of proteins and lipids that would otherwise have been removed from the Golgi by AP-3.

In conclusion, our study revealed that, despite lacking the ear domains characteristic of AP-1 and AP-2 complexes, the unstructured hinges of the δ (Apl5) and $\beta 3$ (Apl6) subunits are essential for AP-3 function in yeast. Truncation of these hinges disrupted AP-3 vesicle budding but did not impair AP-3 complex recruitment to the Golgi, indicating a role for the intrinsically disordered hinges in vesicle formation and/or fission. Further investigation into the biophysical properties and potential

interactors of AP-3 hinge regions, and the interplay between AP-3 and other Golgi-associated proteins, will be crucial to understanding the mechanism of AP-3-mediated cargo sorting and its effects on Golgi maturation.

MATERIALS AND METHODS

Computational modeling

Ribbon structures of the four adaptor protein subunits in each of the AP-1, AP-2, or AP-3 complexes in *S. cerevisiae* or in humans were generated by the predictive algorithm, AlphaFold2 (Jumper et al., 2021). Molecular graphics and analyses of these structures were performed with UCSF ChimeraX (Meng et al., 2023), developed by the Resource for Biocomputing, Visualization, and Informatics at the University of California, San Francisco, with support from National Institutes of Health R01-GM129325 and the Office of Cyber Infrastructure and Computational Biology, National Institute of Allergy and Infectious Diseases. IDRs in the Apl5 and Apl6 protein sequences were identified using the Metapredict algorithm (Emenecker et al., 2021).

Construction of yeast strains and DNA plasmids

Standard techniques were used for the growth and genetic manipulation of *S. cerevisiae* strains (Table S1) and for the construction of plasmids (Table S2). Yeast strains created for this study were constructed by one-step PCR-based integration (Longtine et al., 1998), with the exception of strains expressing C-terminal GFP-tagged Apl5 or Apl6, which were created by chromosomal integration of linearized plasmids YIplac211-APL5-iGFPx6 or YIplac211-APL6-msGFPx3 (Day et al., 2018). Strains expressing the AP-3 synthetic cargo, GNSS, were also created by chromosomal integration of plasmid pLC1514 linearized using NotI-SnaBI, which integrates at the *SUC2* locus. All yeast strains in this study were authenticated by PCR analysis of genomic DNA. The wild-type *APL5* or *APL6* gene was cloned into the pRS416 yeast shuttle vector (Sikorski and Hieter, 1989) using the Gibson cloning method. The cloned *APL5* gene included 1000 bp of promoter sequence and 312 bp of terminator sequence. The cloned *APL6* gene included 571 bp of promoter sequence and 779 bp of terminator sequence. pRS416 plasmids encoding the series of truncation-mutant *apl5* or *apl6* alleles were created by introducing nonsense mutations in the corresponding wild-type gene using QuikChange mutagenesis (Agilent Technologies, Santa Clara, CA). Bacterial expression plasmids encoding GST fused to hinge regions of different AP large subunits were constructed by PCR amplification of each region, digestion of each PCR product with NcoI and BamHI, and ligation of each digested product

with NcoI- and BamHI-digested pGST-Parallel (Sheffield et al., 1999). All yeast and DNA reagents are available upon request.

Yeast cell growth assays

The effects of adaptor subunit gene deletions on the growth of yeast strains expressing the wild-type *CHC1* gene or the temperature-sensitive *chc1-521* allele were performed as described previously (Yeung et al., 1999). Yeast cultures were grown overnight to saturation and adjusted the next day to the same density (1 OD₆₀₀/ml), then serially diluted 10-fold, and cells (5 µl) were spotted onto growth medium. Each plate was incubated at 24°C, 30°C, or 37°C for two days before imaging.

Protein purification and binding assays

Escherichia coli strain BL21(DE3) was transformed with different pGST-Parallel vectors encoding GST-hinge regions. Protein expression was induced by the addition of isopropyl β-D-1-thiogalactopyranoside to a final concentration of 200 µM. Cells were pelleted and resuspended in 40 mL of PBS buffer (phosphate buffered saline (pH 7.4), 1 mM DTT, 1 mM PMSF, 1 µg/ml leupeptin, 1 µg/ml pepstatin), and ~700 µL was supplemented with 0.5% Triton X-100 and 10 µg DNase I, then lysed by sonication, and centrifuged at 20,000 x g for 20 min to produce clarified bacterial lysate, 500 µL of which was added to 50 µL Glutathione Sepharose 4B (Amersham Biosciences, Piscataway, NJ) and rotated overnight at 4°C, then washed thrice with 500 µL PBS, thrice with 500 µL PBS +350 mM NaCl, and thrice with 500 µL yeast lysis buffer (20 mM HEPES pH 6.8, 0.2 M Sorbitol, 2 mM EDTA, 50 mM potassium acetate, 1 µg/mL aprotinin, 1 µg/mL leupeptin, 1 µg/mL pepstatin, 1 µg/mL Pefabloc-SC (AEBSF), 1 mM PMSF). Washed GST resin was then added to 500 µL (150 OD₆₀₀ units) of yeast extract produced by supplementing clarified yeast cell lysate prepared from 1 L cultures of yeast cells prepared as follows: yeast cells were pelleted by centrifugation, converted to spheroplasts, then gently sedimented at 1,000 x g for 2 min, and the pellet was resuspended in yeast lysis buffer and homogenized by 25 strokes in a 15-ml tissue grinder/Dounce homogenizer; to produce clarified yeast cell lysate in which unlysed cells were removed by sedimentation at 1,000 x g for 5 min. GST affinity resin was incubated with yeast lysate for 1 hr at 4°C, then washed thrice with ice-cold yeast lysis buffer before incubating with 50 µL glutathione elution buffer (50 mM Tris-Cl pH 7.9, 20 mM reduced glutathione, 600 mM NaCl, 1% Triton X-100) for 10 min on ice. Two elutions were pooled and resolved by SDS polyacrylamide gel electrophoresis. Gels were stained with Coomassie Brilliant Blue G or transferred to nitrocellulose and imaged by western blot using rabbit antiserum against yeast clathrin heavy chain (Lemmon et al., 1998).

Invertase activity assays

Extracellular invertase activity secreted by cells growing on solid support was performed by spotting cells as described above to agar medium in which fructose was substituted in place of glucose as the carbon source. The cells were incubated at 26°C for two days before being overlaid with top agar containing a chromogenic solution (125 mM sucrose [ultrapure], 166 mM sodium acetate [pH 5.2], 0.666 mM *N*-ethylmaleimide, 0.017 mg/mL horseradish peroxidase, 15 units/mL glucose oxidase, 1 mg/mL *o*-dianisidine, 3% agar [w/v]). Secreted invertase activity is observed as a color change from white to reddish-brown within ~15 min (Darsow et al., 2000). Quantitation of secreted invertase activity was assayed by centrifuging 0.4 OD₆₀₀ units of cells grown in culture to mid-logarithmic density and washing the cells twice in 100 mM sodium acetate (pH 5.2) before resuspending them in 400 µL 100 mM sodium acetate (pH 5.2). These samples were then split into two groups of 190µL each, one to measure extracellular invertase activity, the other to measure total invertase activity, using the liquid invertase assay described in Darsow, et al. (2000). Quantitative measurements of the amount of secreted invertase activity were performed in triplicate in at least three independent experiments.

Fluorescence microscopy

Liquid yeast cultures were grown to mid-log phase before staining the vacuole lumen using CMAC blue stain (ThermoFisher Scientific) for 20 min in YPD and then rinsed prior to imaging. For conventional spinning disk confocal fluorescence microscopy, live yeast cells were observed at room temperature with an inverted fluorescence microscope (Ti2 2E PSF; Nikon) equipped with a Yokogawa CSU-X1 spinning disk confocal system and a 100X (1.45 numerical aperture) oil objective (Plan Apo λ; Nikon). Images taken with an Andor iXON Ultra 512x512 EMCCD camera were acquired with Micromanager version 2.0 software and analyzed with ImageJ software (NIH). For super-resolution spinning disk confocal microscopy, live cells were imaged at room temperature with an inverted fluorescence scope (Ti2 2E PSF; Nikon) equipped with a Yokogawa CSU-W1SoRa (Super-resolution through Optical Reassignment) spinning disc confocal system and a 60X (1.42 numerical aperture) oil objective (Plan Apo λD; Nikon). Images were acquired in NikonElements using a Hamamatsu ORCA-FUSION-BT C15540 camera and magnified using the intermediate 2.8X magnifier. These images were then deconvolved using NikonElements 3D deconvolution package and analyzed further using ImageJ software. Colocalization frequency in super-resolution images was performed by max-projecting three Z-stacks at 0.5 µm spacing. The projected images were normalized to a set of wild-type images for fluorescence intensity. ImageJ thresholding was used to generate masks of cell boundaries and outline the puncta of proteins of interest. These masks were used to measure pixel overlap of proteins of interest, puncta abundance, and puncta size of each channel. Colocalization events were quantified relative to each channel and were filtered for >5% pixel overlap

before quantifying. At least 200 cells were sampled for each experimental condition. Each condition was repeated on separate days for at least three experimental replicates, and the standard error of the mean was calculated. Statistical significance was calculated in GraphPad Prism software using paired and non-paired Student's *t* test, as appropriate.

For VAEF/HiLo microscopy, yeast samples were seeded onto agarose pads as described previously (Rines et al., 2011). Spinning disk and high-speed images were acquired using a Nikon Ti2 frame with a Mad City piezoelectric Z-stage and a 100x 1.45 NA Plan Apochromat objective. High-speed imaging was done with a Toptica iChrome MLE laser combiner and launch, 488 and 561 nm diode lasers (Coherent), a Gataca Systems iLas2 laser aiming module operated in 360° HiLo mode, a Cairn OpoSplit II Bypass emission splitting unit, a custom filter and dichroic mirror set (Chroma, Brattleboro, Vermont) and a Photometrics Prime 95B sCMOS camera operated at frame rates of 20-80 Hz. Pixel spacing at the sample focal plane, with a 1.5× tube lens, was 73 nm. Images were deconvolved using NikonElements software to reduce noise, and analyzed using Image/J. Particle tracking for fluorescent proteins was performed using the Image/J TrackMate plugin (Ershov et al., 2022). Particle tracks were filtered using a threshold of at least 20 persistent frames (1 second) before quantifying. Track maps and data were exported to .xml files and then analyzed in MATLAB using the @msdalyzer tool to generate the mean squared displacement (MSD) graphs presented in Fig. 4C,D) (Tarantino et al., 2014). Vesicle tracks from at least 30 cells per experimental condition were used to generate the MSD graphs and confidence intervals. The data were acquired in three independent experiments over several days.

Electron microscopy

Liquid cultures of yeast cells were harvested at mid-log phase, vacuum-filtered on 0.45- μ m millipore paper, loaded into 0.5-mm aluminum hats, and high pressure frozen with a Wohlwend HPF (Wohlwend, Switzerland). Cells were freeze-substituted in an Automated Freeze-Substitution machine (AFS, Leica Vienna, Austria) at -90°C in an en bloc preparation of 0.1% uranyl acetate and 0.25% glutaraldehyde in anhydrous acetone. Samples were then washed in pure anhydrous acetone, embedded in Lowicryl HM20 resin (Polysciences, Warrington, PA), and UV-polymerized at -60°C before warming slowly over 4 days to room temperature (RT). The sample blocks were then stored at -20°C . These methods preserve membrane and protein structure and provide consistent en bloc staining for immuno-EM membrane identification (Giddings, 2003).

A Leica UC6 Ultra-Microtome was used to cut and place serial sections on Formvar-coated rhodium-plated copper slot grids (Electron Microscopy Sciences). 80- to 90-nm serial sections were cut for transmission electron microscopy (TEM) and immuno-EM experiments and 200-nm thick

serial sections were cut for dual-axis tomography. For immunolabeling experiments, grids were exposed to sequential 50 μ L droplets. Nonspecific antibody binding was blocked by incubation with 1% PBS + 1% dry milk (blocking solution) for 20 min at RT, then exposed to primary antibodies overnight at 4°C (1:200 anti-GFP) in blocking solution, washed at RT in 1% PBS with 3 sequential 50 μ L drops, labeled with a secondary anti-rabbit or anti-mouse gold (depending on the primary antibody used) at RT for 1 hour (1:100 goat-anti-rabbit, Electron Microscopy Sciences), washed in 1% PBS with 3 sequential 50 μ L drops, and finally washed in distilled water with 2 sequential 50 μ L drops.

Immuno-EM sections were imaged with a FEI Tecnai T12 Spirit electron microscope equipped with a 120 kV LaB6 filament and AMT (2 k \times 2 k) CCD. Images from a hundred randomly oriented cells per strain were used to quality-control freezing, embedding, and staining. Thick sections were labeled with fiduciary 15-nm colloidal gold (British Biocell International) on both sides and tilt imaged with a Tecnai 30 (f-30, 300 kV; FEI-Company, Eindhoven, the Netherlands) with dual-tilt series images collected from +60° to -60° with 1.5° increments using a Gatan US4000 4k \times 4k CCD camera (Abingdon, United Kingdom). The tilt series were imaged primarily at 19,000 \times magnification and repeated with a 90° rotation for dual-axis tomography (Mastronarde 1997). Tomograms were built and modeled using the IMOD software package (Kremer et al., 1996) using an iMac (Apple). Golgi, vacuoles, and cytosolic vesicle models from tomograms were manually assigned from the outer leaflet every 5 nm. Videos were made using IMOD and QuickTime Pro (Apple). Data were analyzed and graphed using Prism 9 (GraphPad).

ACKNOWLEDGEMENTS

The authors want to thank Ayla Nack and Rick Trippe (U. Colorado) for providing technical support and Elizabeth Conibear (U. British Columbia) for providing the integrative plasmid encoding GNSS.

COMPETING INTERESTS

The authors declare no competing interests exist.

FUNDING

This work was supported by the National Institutes of Health/National Institute of General Medical Sciences grant number R01 GM130644 (to GO and AM) and grant number R35 GM149202 (to GO).

REFERENCES

- Aguet, F., Antonescu, C. N., Mettlen, M., Schmid, S. L. and Danuser, G.** (2013). Advances in Analysis of Low Signal-to-Noise Images Link Dynamin and AP2 to the Functions of an Endocytic Checkpoint. *Developmental Cell* **26**, 279–291.
- Angers, C. G. and Merz, A. J.** (2009). HOPS Interacts with Apl5 at the Vacuole Membrane and Is Required for Consumption of AP-3 Transport Vesicles. *MBoC* **20**, 4563–4574.
- Angers, C. G. and Merz, A. J.** (2011). New links between vesicle coats and Rab-mediated vesicle targeting. *Seminars in Cell & Developmental Biology* **22**, 18–26.
- Asensio, C. S., Sirkis, D. W., Maas, J. W., Egami, K., To, T.-L., Brodsky, F. M., Shu, X., Cheng, Y. and Edwards, R. H.** (2013). Self-Assembly of VPS41 Promotes Sorting Required for Biogenesis of the Regulated Secretory Pathway. *Developmental Cell* **27**, 425–437.
- Bankaitis, V. A., Johnson, L. M. and Emr, S. D.** (1986). Isolation of yeast mutants defective in protein targeting to the vacuole. *Proceedings of the National Academy of Sciences* **83**, 9075–9079.
- Begley, M., Aragon, M. and Baker, R. W.** (2024). A structure-based mechanism for initiation of AP-3 coated vesicle formation. *bioRxiv* doi: 2024.06.05.597630.
- Black, M. W. and Pelham, H. R.** (2000). A selective transport route from Golgi to late endosomes that requires the yeast GGA proteins. *J Cell Biol* **151**, 587–600.
- Bowman, S. L., Bi-Karchin, J., Le, L. and Marks, M. S.** (2019). The road to lysosome-related organelles: Insights from Hermansky-Pudlak syndrome and other rare diseases. *Traffic* **20**, 404–435.
- Bui, Q. T., Golinelli-Cohen, M.-P. and Jackson, C. L.** (2009). Large Arf1 guanine nucleotide exchange factors: evolution, domain structure, and roles in membrane trafficking and human disease. *Mol Genet Genomics* **282**, 329–350.
- Cabrera, M., Langemeyer, L., Mari, M., Rethmeier, R., Orban, I., Perz, A., Bröcker, C., Griffith, J., Klose, D., Steinhoff, H.-J., et al.** (2010). Phosphorylation of a membrane curvature-sensing motif switches function of the HOPS subunit Vps41 in membrane tethering. *Journal of Cell Biology* **191**, 845–859.
- Casanova, J. E.** (2007). Regulation of Arf activation: the Sec7 family of guanine nucleotide exchange factors. *Traffic* **8**, 1476–1485.

Casler, J. C. and Glick, B. S. (2020). A microscopy-based kinetic analysis of yeast vacuolar protein sorting. *eLife* **9**, e56844.

Casler, J. C., Papanikou, E., Barrero, J. J. and Glick, B. S. (2019). Maturation-driven transport and AP-1–dependent recycling of a secretory cargo in the Golgi. *Journal of Cell Biology* **218**, 1582–1601.

Casler, J. C., Johnson, N., Krahn, A. H., Pantazopoulou, A., Day, K. J. and Glick, B. S. (2021). Clathrin adaptors mediate two sequential pathways of intra-Golgi recycling. *Journal of Cell Biology* **221**, e202103199.

Cowles, C. R., Odorizzi, G., Payne, G. S. and Emr, S. D. (1997a). The AP-3 Adaptor Complex Is Essential for Cargo-Selective Transport to the Yeast Vacuole. *Cell* **91**, 109–118.

Cowles, C. R., Snyder, W. B., Burd, C. G. and Emr, S. D. (1997b). Novel Golgi to vacuole delivery pathway in yeast: identification of a sorting determinant and required transport component. *The EMBO Journal* **16**, 2769–2782.

Daboussi, L., Costaguta, G. and Payne, G. S. (2012). Phosphoinositide-mediated clathrin adaptor progression at the trans-Golgi network. *Nat Cell Biol* **14**, 239–248.

Darsow, T., Odorizzi, G. and Emr, S. D. (2000). Invertase fusion proteins for analysis of protein trafficking in yeast. In *Methods in Enzymology* (ed. Thorner, J.), Emr, S. D.), and Abelson, J. N.), pp. 95–106. Academic Press.

Darsow, T., Katzmann, D. J., Cowles, C. R. and Emr, S. D. (2001). Vps41p Function in the Alkaline Phosphatase Pathway Requires Homo-oligomerization and Interaction with AP-3 through Two Distinct Domains. *MBoC* **12**, 37–51.

Day, K. J., Casler, J. C. and Glick, B. S. (2018). Budding Yeast Has a Minimal Endomembrane System. *Dev Cell* **44**, 56-72.e4.

Dell'Angelica, E. C. (2001). Clathrin-binding proteins: got a motif? Join the network! *Trends Cell Biol* **11**, 315–318.

Dell'Angelica, E. C. (2009). AP-3-dependent trafficking and disease: the first decade. *Current Opinion in Cell Biology* **21**, 552–559.

Dell'Angelica, E. C., Ooi, C. E. and Bonifacino, J. S. (1997). β 3A-adaptin, a Subunit of the Adaptor-like Complex AP-3 *. *Journal of Biological Chemistry* **272**, 15078–15084.

Dell'Angelica, E. C., Klumperman, J., Stoorvogel, W. and Bonifacino, J. S. (1998). Association of the AP-3 Adaptor Complex with Clathrin. *Science* **280**, 431–434.

Dell'Angelica, E. C., Puertollano, R., Mullins, C., Aguilar, R. C., Vargas, J. D., Hartnell, L. M. and Bonifacino, J. S. (2000). GGAs: a family of ADP ribosylation factor-binding proteins related to adaptors and associated with the Golgi complex. *J Cell Biol* **149**, 81–94.

Drake, M. T., Zhu, Y. and Kornfeld, S. (2000). The assembly of AP-3 adaptor complex-containing clathrin-coated vesicles on synthetic liposomes. *Mol Biol Cell* **11**, 3723–3736.

D'Souza-Schorey, C. and Chavrier, P. (2006). ARF proteins: roles in membrane traffic and beyond. *Nat Rev Mol Cell Biol* **7**, 347–358.

Edeling, M. A., Smith, C. and Owen, D. (2006). Life of a clathrin coat: insights from clathrin and AP structures. *Nat Rev Mol Cell Biol* **7**, 32–44.

Emenecker, R. J., Griffith, D. and Holehouse, A. S. (2021). Metapredict: a fast, accurate, and easy-to-use predictor of consensus disorder and structure. *Biophysical Journal* **120**, 4312–4319.

Franzusoff, A., Redding, K., Crosby, J., Fuller, R. S. and Schekman, R. (1991). Localization of components involved in protein transport and processing through the yeast Golgi apparatus. *J Cell Biol* **112**, 27–37.

Goldberg, J. (1999). Structural and functional analysis of the ARF1-ARFGAP complex reveals a role for coatomer in GTP hydrolysis. *Cell* **96**, 893–902.

Heuser, J. E. and Keen, J. (1988). Deep-etch visualization of proteins involved in clathrin assembly. *J Cell Biol* **107**, 877–886.

Highland, C. M. and Fromme, J. C. (2021). Arf1 directly recruits the Pik1-Frq1 PI4K complex to regulate the final stages of Golgi maturation. *MBoC* **32**, 1064–1080.

Hirst, J., Lui, W. W., Bright, N. A., Totty, N., Seaman, M. N. and Robinson, M. S. (2000). A family of proteins with gamma-adaptin and VHS domains that facilitate trafficking between the trans-Golgi network and the vacuole/lysosome. *J Cell Biol* **149**, 67–80.

Hirst, J., Barlow, L. D., Francisco, G. C., Sahlender, D. A., Seaman, M. N. J., Dacks, J. B. and Robinson, M. S. (2011). The Fifth Adaptor Protein Complex. *PLoS Biology* **9**, e1001170.

Horwitz, M., Benson, K. F., Duan, Z., Li, F.-Q. and Person, R. E. (2004). Hereditary neutropenia: dogs explain human neutrophil elastase mutations. *Trends in Molecular Medicine* **10**, 163–170.

Jumper, J., Evans, R., Pritzel, A., Green, T., Figurnov, M., Ronneberger, O., Tunyasuvunakool, K., Bates, R., Žídek, A., Potapenko, A., et al. (2021). Highly accurate protein structure prediction with AlphaFold. *Nature* **596**, 583–589.

Kirchhausen, T., Owen, D. and Harrison, S. C. (2014). Molecular Structure, Function, and Dynamics of Clathrin-Mediated Membrane Traffic. *Cold Spring Harb Perspect Biol* **6**, a016725.

Konopka, C. A. and Bednarek, S. Y. (2008). Variable-angle epifluorescence microscopy: a new way to look at protein dynamics in the plant cell cortex. *Plant J* **53**, 186–196.

Kremer, J. R., Mastrorarde, D. N. and McIntosh, J. R. (1996). Computer visualization of three-dimensional image data using IMOD. *J Struct Biol* **116**, 71–76.

Lemmon, S., Lemmon, V. P. and Jones, E. W. (1988). Characterization of yeast clathrin and anticlathrin heavy-chain monoclonal antibodies. *J Cell Biochem* **36**, 329–340.

Longtine, M. S., Iii, A. M., Demarini, D. J., Shah, N. G., Wach, A., Brachat, A., Philippsen, P. and Pringle, J. R. (1998). Additional modules for versatile and economical PCR-based gene deletion and modification in *Saccharomyces cerevisiae*. *Yeast* **14**, 953–961.

Losev, E., Reinke, C. A., Jellen, J., Strongin, D. E., Bevis, B. J. and Glick, B. S. (2006). Golgi maturation visualized in living yeast. *Nature* **441**, 1002–1006.

Marcusson, E. G., Horazdovsky, B. F., Cereghino, J. L., Gharakhanian, E. and Emr, S. D. (1994). The sorting receptor for yeast vacuolar carboxypeptidase Y is encoded by the VPS10 gene. *Cell* **77**, 579–586.

Martzoukou, O., Amillis, S., Zervakou, A., Christoforidis, S. and Diallinas, G. (2017). The AP-2 complex has a specialized clathrin-independent role in apical endocytosis and polar growth in fungi. *eLife* **6**, e20083.

Mastrorarde, D. N. (1997). Dual-axis tomography: an approach with alignment methods that preserve resolution. *J Struct Biol* **120**, 343–352.

Morgan, T. H. (1910). Sex limited inheritance in *Drosophila*. *Science* **32**, 120–122.

Motley, A. M., Berg, N., Taylor, M. J., Sahlender, D. A., Hirst, J., Owen, D. J. and Robinson, M. S. (2006). Functional Analysis of AP-2 α and $\mu 2$ Subunits. *MBoC* **17**, 5298–5308.

Newman, L. S., McKeever, M. O., Okano, H. J. and Darnell, R. B. (1995). Beta-NAP, a cerebellar degeneration antigen, is a neuron-specific vesicle coat protein. *Cell* **82**, 773–783.

Ooi, C. E., Dell’Angelica, E. C. and Bonifacino, J. S. (1998). ADP-Ribosylation factor 1 (ARF1) regulates recruitment of the AP-3 adaptor complex to membranes. *J Cell Biol* **142**, 391–402.

Owen, D. J., Vallis, Y., Noble, M. E., Hunter, J. B., Dafforn, T. R., Evans, P. R. and McMahon, H. T. (1999). A structural explanation for the binding of multiple ligands by the alpha-adaptin appendage domain. *Cell* **97**, 805–815.

Peden, A. A., Rudge, R. E., Lui, W. W. Y. and Robinson, M. S. (2002). Assembly and function of AP-3 complexes in cells expressing mutant subunits. *Journal of Cell Biology* **156**, 327–336.

Peden, A. A., Oorschot, V., Hesser, B. A., Austin, C. D., Scheller, R. H. and Klumperman, J. (2004). Localization of the AP-3 adaptor complex defines a novel endosomal exit site for lysosomal membrane proteins. *J Cell Biol* **164**, 1065–1076.

Peyroche, A., Paris, S. and Jackson, C. L. (1996). Nucleotide exchange on ARF mediated by yeast Gea1 protein. *Nature* **384**, 479–481.

Plemel, R. L., Odorizzi, G. and Merz, A. J. (2021). Genetically encoded multimode reporter of adaptor complex 3 traffic in budding yeast. *Traffic* **22**, 38–44.

Poon, P. P., Nothwehr, S. F., Singer, R. A. and Johnston, G. C. (2001). The Gcs1 and Age2 ArfGAP proteins provide overlapping essential function for transport from the yeast trans-Golgi network. *Journal of Cell Biology* **155**, 1239–1250.

- Praefcke, G. J. K., Ford, M. G. J., Schmid, E. M., Olesen, L. E., Gallop, J. L., Peak-Chew, S.-Y., Vallis, Y., Babu, M. M., Mills, I. G. and McMahon, H. T.** (2004). Evolving nature of the AP2 alpha-appendage hub during clathrin-coated vesicle endocytosis. *EMBO J* **23**, 4371–4383.
- Puertollano, R., Randazzo, P. A., Presley, J. F., Hartnell, L. M. and Bonifacino, J. S.** (2001). The GGAs promote ARF-dependent recruitment of clathrin to the TGN. *Cell* **105**, 93–102.
- Reggiori, F., Black, M. W. and Pelham, H. R. B.** (2000). Polar Transmembrane Domains Target Proteins to the Interior of the Yeast Vacuole. *MBoC* **11**, 3737–3749.
- Rehling, P., Darsow, T., Katzmann, D. J. and Emr, S. D.** (1999). Formation of AP-3 transport intermediates requires Vps41 function. *Nat Cell Biol* **1**, 346–353.
- Reis, C. R., Chen, P., Srinivasan, S., Aguet, F., Mettlen, M. and Schmid, S. L.** (2015). Crosstalk between Akt/GSK3 β signaling and dynamin-1 regulates clathrin-mediated endocytosis. *The EMBO Journal* **34**, 2132–2146.
- Ritter, B., Denisov, A. Y., Philie, J., Deprez, C., Tung, E. C., Gehring, K. and McPherson, P. S.** (2004). Two WXXF-based motifs in NECAPs define the specificity of accessory protein binding to AP-1 and AP-2. *EMBO J* **23**, 3701–3710.
- Robinson, M. S.** (2015). Forty Years of Clathrin-coated Vesicles. *Traffic* **16**, 1210–1238.
- Robinson, M. S., Antrobus, R., Sanger, A., Davies, A. K. and Gershlick, D. C.** (2024). The role of the AP-1 adaptor complex in outgoing and incoming membrane traffic. *Journal of Cell Biology* **223**, e202310071.
- Salazar, G., Zlatic, S., Craige, B., Peden, A. A., Pohl, J. and Faundez, V.** (2009). Hermansky-Pudlak Syndrome Protein Complexes Associate with Phosphatidylinositol 4-Kinase Type II α in Neuronal and Non-neuronal Cells *. *Journal of Biological Chemistry* **284**, 1790–1802.
- Sata, M., Donaldson, J. G., Moss, J. and Vaughan, M.** (1998). Brefeldin A-inhibited guanine nucleotide-exchange activity of Sec7 domain from yeast Sec7 with yeast and mammalian ADP ribosylation factors. *Proc Natl Acad Sci U S A* **95**, 4204–4208.

- Schmid, E. M., Ford, M. G. J., Burtey, A., Praefcke, G. J. K., Peak-Chew, S.-Y., Mills, I. G., Benmerah, A. and McMahon, H. T.** (2006). Role of the AP2 beta-appendage hub in recruiting partners for clathrin-coated vesicle assembly. *PLoS Biol* **4**, e262.
- Schoppe, J., Mari, M., Yavavli, E., Auffarth, K., Cabrera, M., Walter, S., Fröhlich, F. and Ungermann, C.** (2020). AP-3 vesicle uncoating occurs after HOPS-dependent vacuole tethering. *The EMBO Journal* **39**, e105117.
- Schoppe, J., Schubert, E., Apelbaum, A., Yavavli, E., Birkholz, O., Stephanowitz, H., Han, Y., Perz, A., Hofnagel, O., Liu, F., et al.** (2021). Flexible open conformation of the AP-3 complex explains its role in cargo recruitment at the Golgi. *Journal of Biological Chemistry* **297**, 101334.
- Schwartz, M. L., Nickerson, D. P., Lobingier, B. T., Plemel, R. L., Duan, M., Angers, C. G., Zick, M. and Merz, A. J.** (2017). Sec17 (α -SNAP) and an SM-tethering complex regulate the outcome of SNARE zippering in vitro and in vivo. *Elife* **6**, e27396.
- Seals, D. F., Eitzen, G., Margolis, N., Wickner, W. T. and Price, A.** (2000). A Ypt/Rab effector complex containing the Sec1 homolog Vps33p is required for homotypic vacuole fusion. *Proc Natl Acad Sci U S A* **97**, 9402–9407.
- Seaman, M. N., Sowerby, P. J. and Robinson, M. S.** (1996). Cytosolic and membrane-associated proteins involved in the recruitment of AP-1 adaptors onto the trans-Golgi network. *J Biol Chem* **271**, 25446–25451.
- Seaman, M. N., McCaffery, J. M. and Emr, S. D.** (1998). A membrane coat complex essential for endosome-to-Golgi retrograde transport in yeast. *J Cell Biol* **142**, 665–681.
- Sheffield, P., Garrard, S. and Derewenda, Z.** (1999). Overcoming Expression and Purification Problems of RhoGDI Using a Family of “Parallel” Expression Vectors. *Protein Expression and Purification* **15**, 34–39.
- Sikorski, R. S. and Hieter, P.** (1989). A system of shuttle vectors and yeast host strains designed for efficient manipulation of DNA in *Saccharomyces cerevisiae*. *Genetics* **122**, 19–27.
- Simpson, F., Bright, N. A., West, M. A., Newman, L. S., Darnell, R. B. and Robinson, M. S.** (1996). A novel adaptor-related protein complex. *Journal of Cell Biology* **133**, 749–760.

Snead, W. T. and Stachowiak, J. C. (2018). Structure Versus Stochasticity-The Role of Molecular Crowding and Intrinsic Disorder in Membrane Fission. *J Mol Biol* **430**, 2293–2308.

Spang, A., Herrmann, J. M., Hamamoto, S. and Schekman, R. (2001). The ADP ribosylation factor-nucleotide exchange factors Gea1p and Gea2p have overlapping, but not redundant functions in retrograde transport from the Golgi to the endoplasmic reticulum. *Mol Biol Cell* **12**, 1035–1045.

Stammes, M. A. and Rothman, J. E. (1993). The binding of AP-1 clathrin adaptor particles to Golgi membranes requires ADP-ribosylation factor, a small GTP-binding protein. *Cell* **73**, 999–1005.

Stepp, J. D., Huang, K. and Lemmon, S. K. (1997). The yeast adaptor protein complex, AP-3, is essential for the efficient delivery of alkaline phosphatase by the alternate pathway to the vacuole. *J Cell Biol* **139**, 1761–1774.

Tarantino, N., Tinevez, J.-Y., Crowell, E. F., Boisson, B., Henriques, R., Mhlanga, M., Agou, F., Israël, A. and Laplantine, E. (2014). TNF and IL-1 exhibit distinct ubiquitin requirements for inducing NEMO-IKK supramolecular structures. *J Cell Biol* **204**, 231–245.

Theos, A. C., Tenza, D., Martina, J. A., Hurbain, I., Peden, A. A., Sviderskaya, E. V., Stewart, A., Robinson, M. S., Bennett, D. C., Cutler, D. F., et al. (2005). Functions of Adaptor Protein (AP)-3 and AP-1 in Tyrosinase Sorting from Endosomes to Melanosomes. *MBoC* **16**, 5356–5372.

Tojima, T., Suda, Y., Ishii, M., Kurokawa, K. and Nakano, A. (2019). Spatiotemporal dissection of the trans-Golgi network in budding yeast. *Journal of Cell Science* **132**, jcs231159.

Traub, L. M., Ostrom, J. A. and Kornfeld, S. (1993). Biochemical dissection of AP-1 recruitment onto Golgi membranes. *J Cell Biol* **123**, 561–573.

Traub, L. M., Downs, M. A., Westrich, J. L. and Fremont, D. H. (1999). Crystal structure of the alpha appendage of AP-2 reveals a recruitment platform for clathrin-coat assembly. *Proc Natl Acad Sci U S A* **96**, 8907–8912.

Traub, L. M. (2005). Common principles in clathrin-mediated sorting at the Golgi and the plasma membrane. *Biochimica et Biophysica Acta (BBA) - Molecular Cell Research* **1744**, 415–437.

Vowels, J. J. and Payne, G. S. (1998). A dileucine-like sorting signal directs transport into an AP-3-dependent, clathrin-independent pathway to the yeast vacuole. *The EMBO Journal* **17**, 2482–2493.

Yeung, B. G., Phan, H. L. and Payne, G. S. (1999). Adaptor Complex-independent Clathrin Function in Yeast. *MBoC* **10**, 3643–3659.

Zhdankina, O., Strand, N. L., Redmond, J. M. and Boman, A. L. (2001). Yeast GGA proteins interact with GTP-bound Arf and facilitate transport through the Golgi. *Yeast* **18**, 1–18.

Zlatic, S. A., Grossniklaus, E. J., Ryder, P. V., Salazar, G., Mattheyses, A. L., Peden, A. A. and Faundez, V. (2013). Chemical-genetic disruption of clathrin function spares adaptor complex 3-dependent endosome vesicle biogenesis. *Mol Biol Cell* **24**, 2378–2388.

Figures

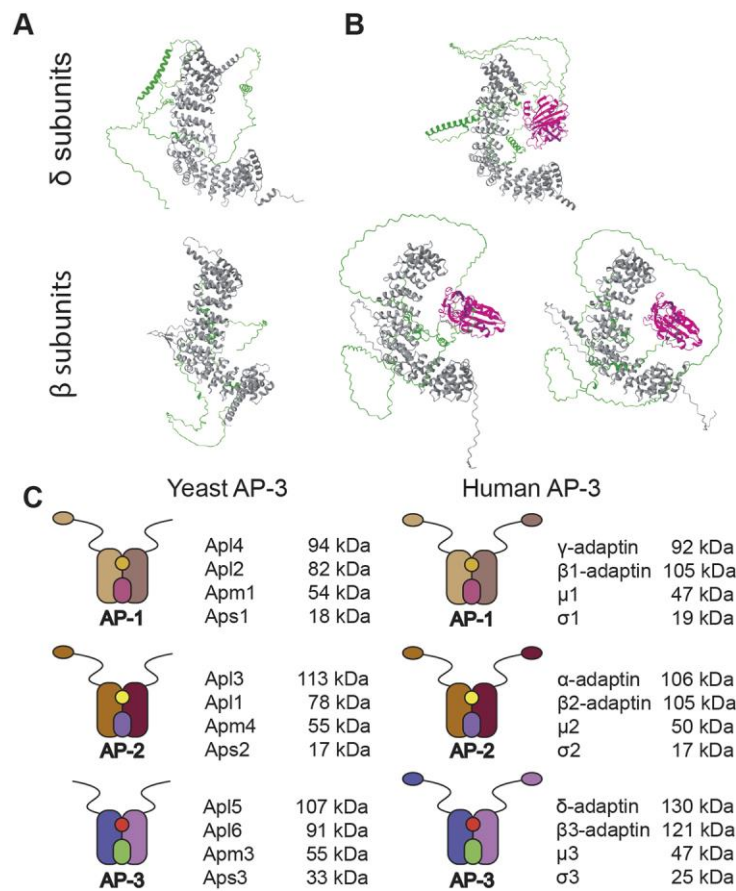


Fig. 1. Folded ear domains are predicted to be missing from yeast AP-3 complexes. A) Yeast AP-3 δ and β 3 subunit structures predicted by AlphaFold2. B) Human AP-3 δ , β 3A, and β 3B subunit structures predicted by AlphaFold2. In (A) and (B), grey coloring indicates the trunk domains of each subunit, while green shows the hinge region; in (B), magenta shows structured ear domains on the C terminus. C) Cartoons of yeast versus human AP-1, AP-2, and AP-3 complexes based on computational modeling.

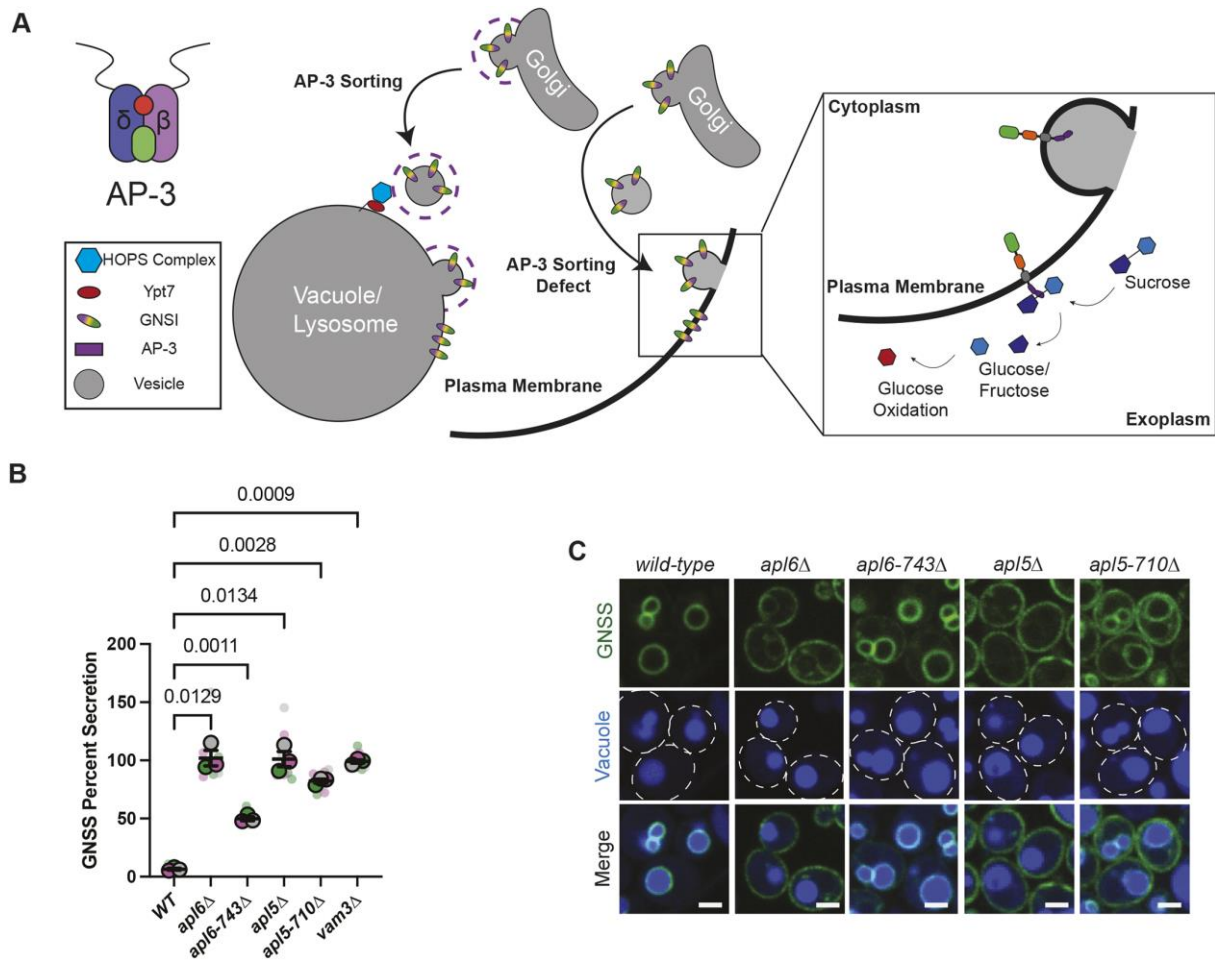


Fig. 2. AP-3 trafficking in yeast requires the hinge region of each AP-3 large subunit. A) Cartoon representation of the synthetic cargo GNSS being sorted via the AP-3 pathway from the Golgi to the vacuole in wild-type yeast and missorted from the Golgi to the plasma membrane in mutant yeast with defects in the AP-3 pathway. B) Comparative secretion of GNSS by liquid invertase assay. The data are representative of three independent experiments. Error bars represent the standard error of the mean (SEM). P-values were calculated using Dunnett's t-test. C) Microscopy showing the localization of GNSS in wild-type and AP-3-mutant cells. The vacuole lumen is stained with CMAC Blue, cell outlines are shown with white dotted lines and scale bars are 2 μ m.

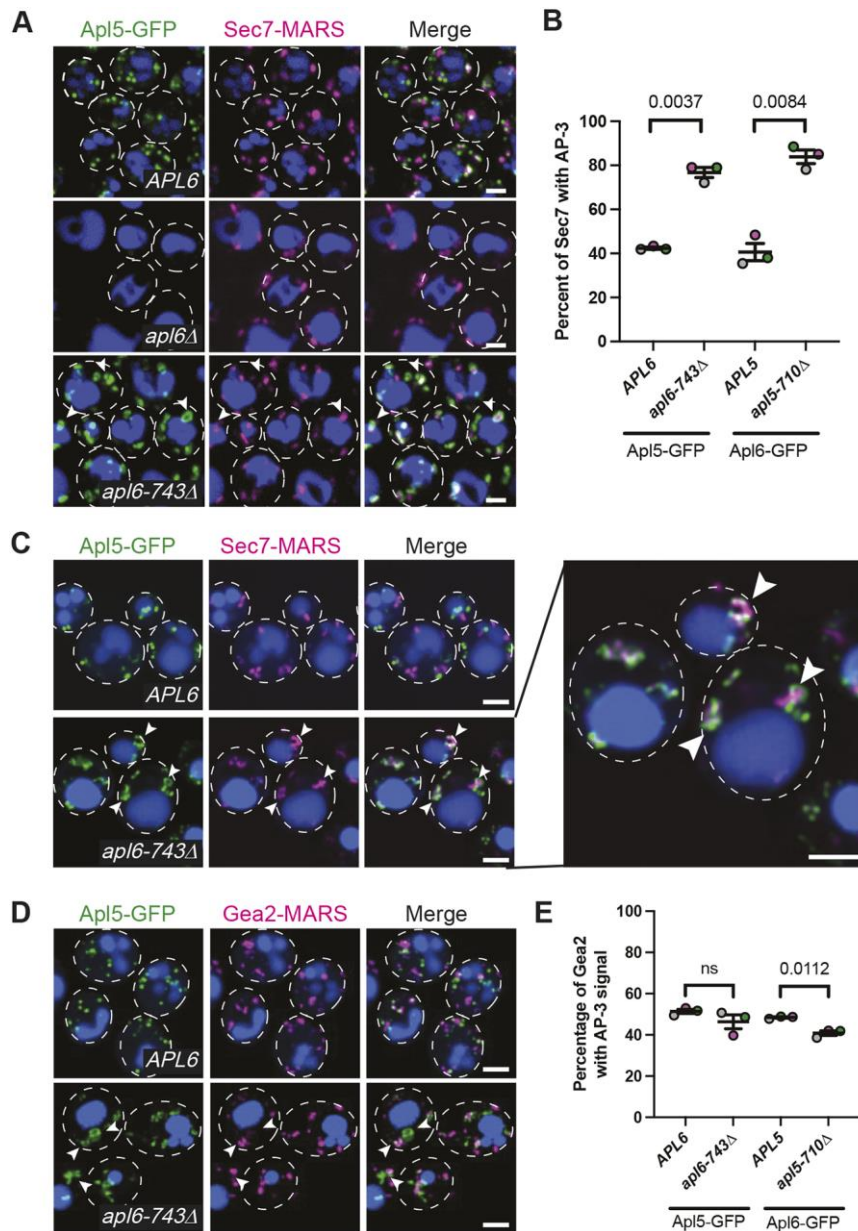


Fig. 3. Hinge truncations inhibit AP-3 vesicle budding from the Golgi. A) Conventional confocal fluorescence microscopy showing GFP-tagged AP-3 localization relative to MARS-Sec7. B) Quantitation of the percentage of Sec7 colocalizing with AP-3 large subunits in wild-type cells and truncation mutants in images obtained by super-resolution confocal fluorescence microscopy. C) Super-resolution confocal fluorescence microscopy showing the distribution of AP-3 relative to Sec7; arrowheads indicate round structures. Right: Zoomed-in image of AP-3 and Sec7 in an AP-3 hinge truncation-mutant cell. D) Super-resolution confocal fluorescence microscopy showing the distribution of AP-3 relative to Gea2; arrowheads indicate round structures. In (A), (C), and (D), the vacuole lumen was stained

with CMAC Blue, cell outlines are shown in white dotted lines, and scale bars are 2 μm . E) Quantitation of the percentage of Gea2 colocalizing with AP-3 large subunits in wild-type and AP-3 truncation-mutant cells in images obtained by super-resolution confocal fluorescence microscopy. In (B) and (E), each point represents the average of at least 200 cells, error bars represent the SEM of three independent experiments, and P-values were determined by paired Student's t-test.

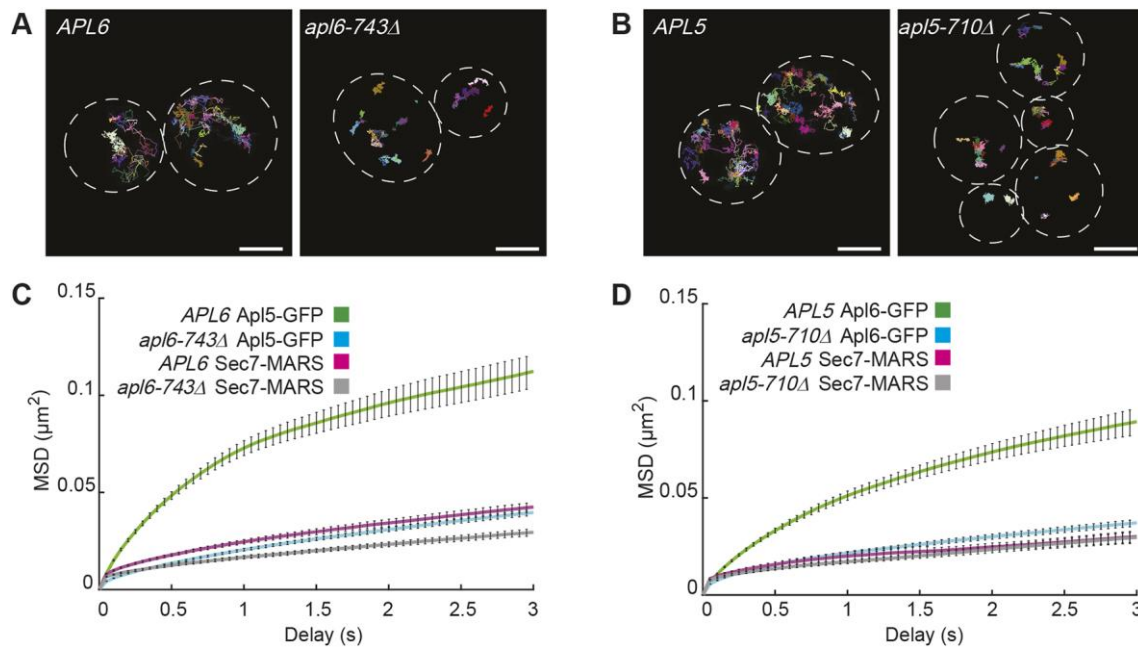


Fig. 4. Hinge truncations inhibit AP-3 vesicle budding. A-B) Track maps of a 30-second movie with 50-ms exposure times, tracking the mobility of Sec7-MARS and either Apl5-GFP (A) or Apl6-GFP (B) in the indicated strains. Scale bars are 2 μm . C-D) Mean squared displacement (MSD) values over three seconds for either (C) Apl5-GFP and Sec7-MARS in yeast expressing either *APL6* or *apl6-743Δ* or (D) Apl6-GFP and Sec7-MARS in cells expressing either *APL5* or *apl5-710Δ*. At least 50 cells were quantified in each group across nine motility assays like those depicted in (A) and (B). Movies were captured on three different days. Error bars represent SEM for puncta displacement at that time.

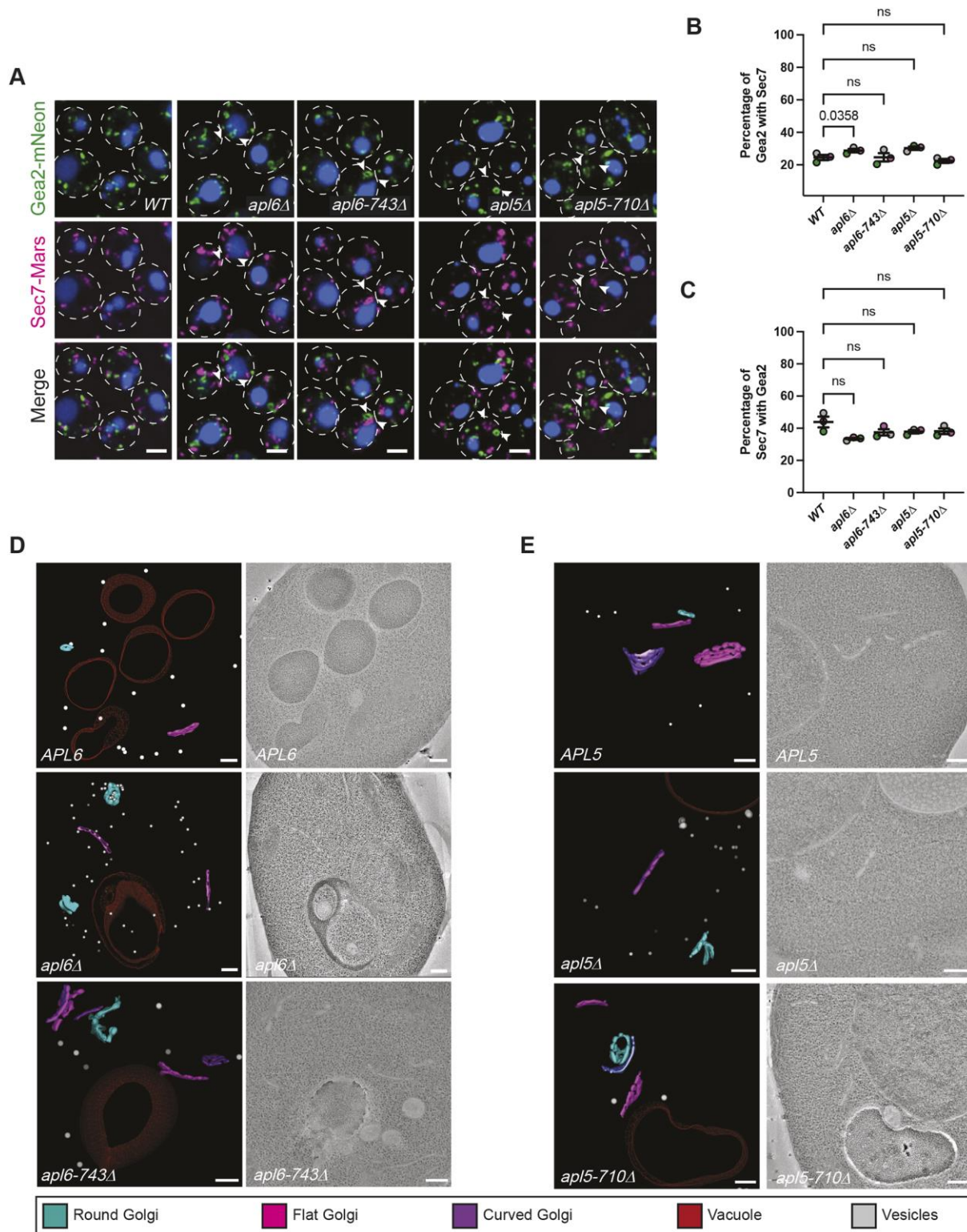


Fig. 5. AP-3 dysfunction alters Golgi morphology. A) Super-resolution confocal fluorescence microscopy showing the effects of AP-3 mutations on the relative localizations of Gea2-mNeon and Sec7-Mars.; scale bars are 2 μ m. B) Graph showing the percentage of Gea2 puncta with Sec7 overlap. C) Graph showing the percent of Sec7 with Gea2 overlap. In

(B) and (C), error bars show SEM, and P-values were determined by Dunett's test. D-E) Tomographic representatives of Golgi morphology changes in wild-type versus *apl6*- or *apl5*-mutant cells. Flat Golgi shown in magenta, round Golgi shown in cyan, curved Golgi shown in purple, vacuole membrane shown in red, and cytosolic vesicles shown in grey. Scale bars in (D) and (E) are 200 nm.

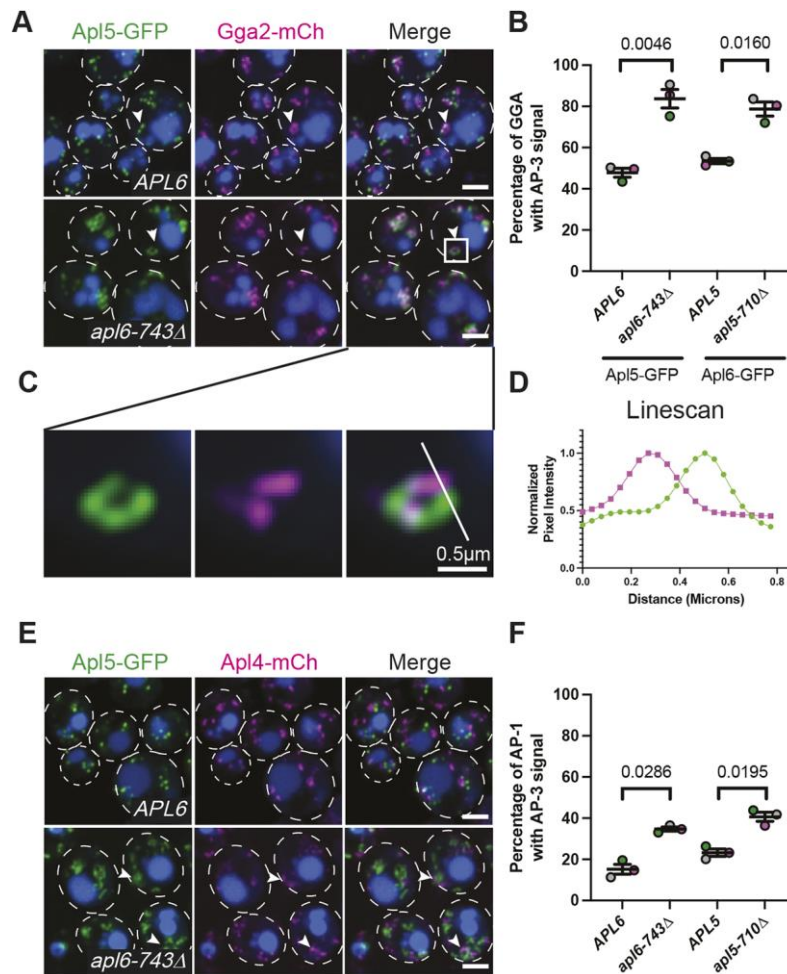


Fig. 6. Budding deficiency causes AP-3 to accumulate at late Golgi compartments. A) Super-resolution confocal fluorescence microscopy showing the distribution of AP-3 relative to Gga2; arrowheads indicate rounded structures for both Gga2 and AP-3. B) Quantitation of the percentage of Gga2 colocalizing with AP-3 large subunits in wild-type AP-3 and truncation-mutant AP-3 cells. C) Zoomed-in image of AP-3 and GGA commingling donuts; scale bar is 0.5 μm. D) Linescan of AP-3 and GGA in an AP-3 truncation mutant. E) Super-resolution confocal fluorescence microscopy showing the distribution of AP-3 relative to AP-1; arrowheads indicate rounded structures for both AP-1 and AP-3. In (A) and (E), the vacuole lumen was stained with CMAC Blue, cell outlines are shown with white dotted lines, and scale bars are 2 μm. F) Quantitation of the percentage of AP-1 colocalizing with AP-3 large subunits in wild-type AP-3 and truncation-mutant AP-3 cells. In (B) and (F), each point represents the average of at least 200 cells, error bars show the SEM, and P-values were determined by paired Student's t-test.

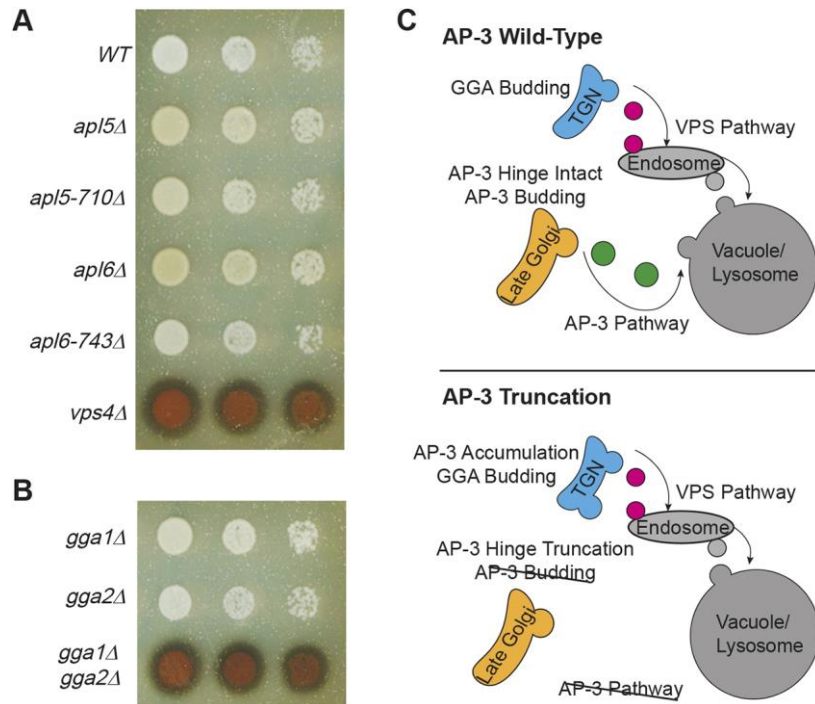


Fig. 7. AP-3 dysfunction does not affect GGA sorting activity. A) Invertase overlay investigating the effects of AP-3 mutations (A) versus GGA mutations (B) on the sorting of CPY-Invertase, which follows the VPS pathway. Each overlay reaction was imaged after 30 min. Cellular concentrations for each strain were 1.0, 0.1, and 0.01 OD₆₀₀ units/ml (left to right). C) Cartoon illustrating the departure of AP-3 vesicles at late Golgi and GGA vesicle departure at the TGN. AP-3 cargoes follow the AP-3 pathway directly to the vacuole, while GGA cargoes follow the VPS pathway (upper panel). When AP-3 hinges are truncated, AP-3 accumulates onto the TGN and AP-3 cargo sorting is perturbed while VPS cargo sorting functions normally (lower panel).

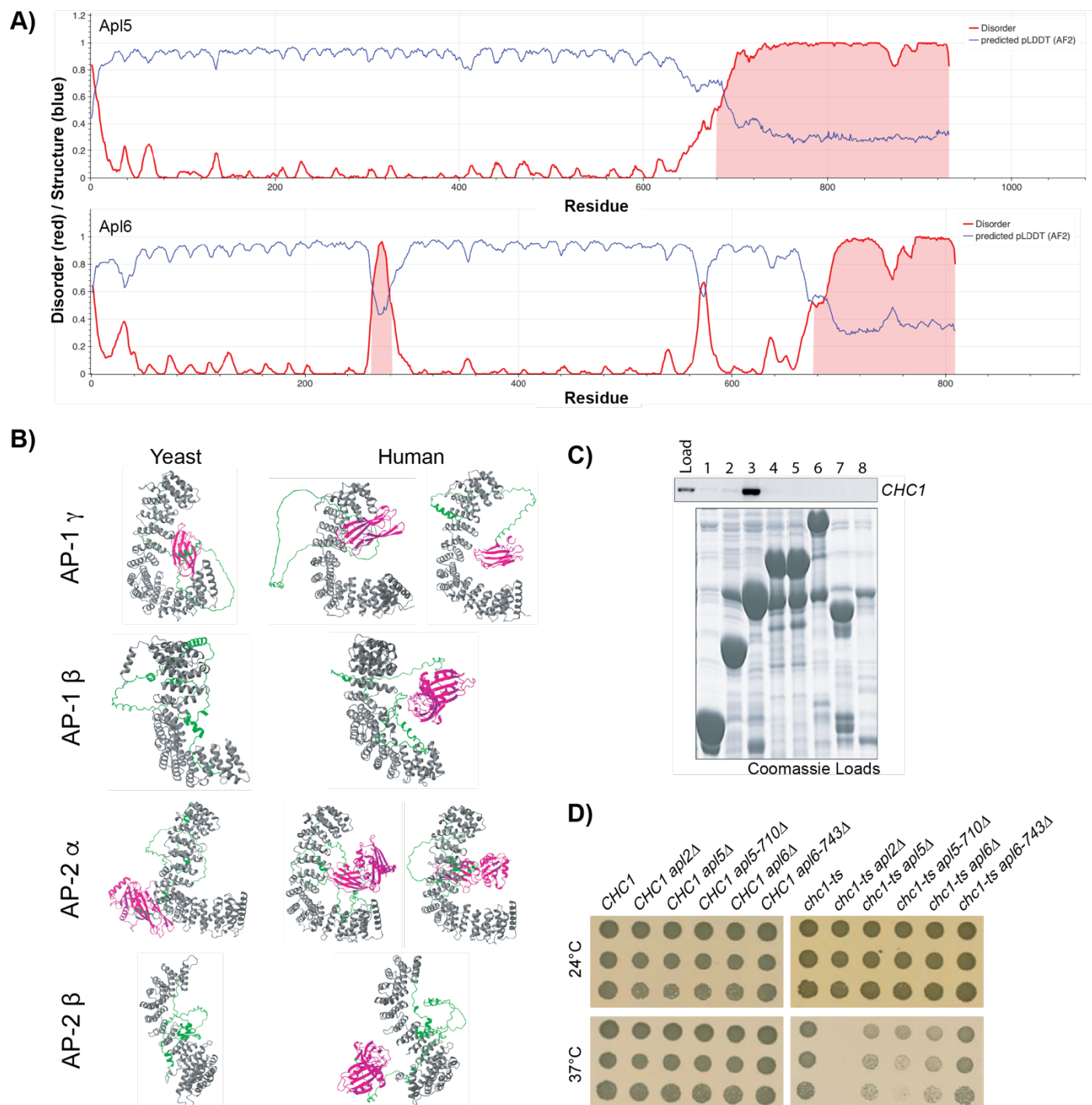


Fig. S1. Ear domains are absent from yeast AP-3 complexes in computational models. A) Metapredict data of Apl5 and Apl6 defining predicted ordered (blue) and disordered regions (red). B) AlphaFold2 predicted structures of large subunits of yeast and human AP-1 and AP-2. Grey coloring indicates the trunk region of each subunit, green shows the hinge regions, and magenta shows the structured ear domain, if predicted. C) Clathrin in yeast lysates binds purified Apl4-hinge (yeast AP-1) fused to GST, but not Apl5-hinge or Apl6-hinge fused to GST. Upper panel shows anti-clathrin heavy chain immunoblot of samples pulled down by glutathione resin after incubation of yeast lysate with each of the GST fusions, as follows: GST only (lane 1), GST-Apl4 amino acids 717-832 (lane 2), GST Apl4 amino acids 662-832 (lane 3), GST-Apl5 amino acids 711-932 (lane 4), GST-Apl5 amino acids 711-932, with the clathrin binding motif-like sequence mutated (lane 5), GST-Apl5 amino acids 615- 932 (lane 6), GST-Apl6 amino acids 673-809 (lane 7), and GST-Apl6 amino acids 625-809 (lane 8). Lower panel, coomassie-stained gel showing the amount of each GST fusion protein used in each pull-down. D) Yeast cell growth assay of the effects of temperature-sensitive clathrin heavy chain mutants when paired with AP complex subunit mutations at 24°C and 37°C.

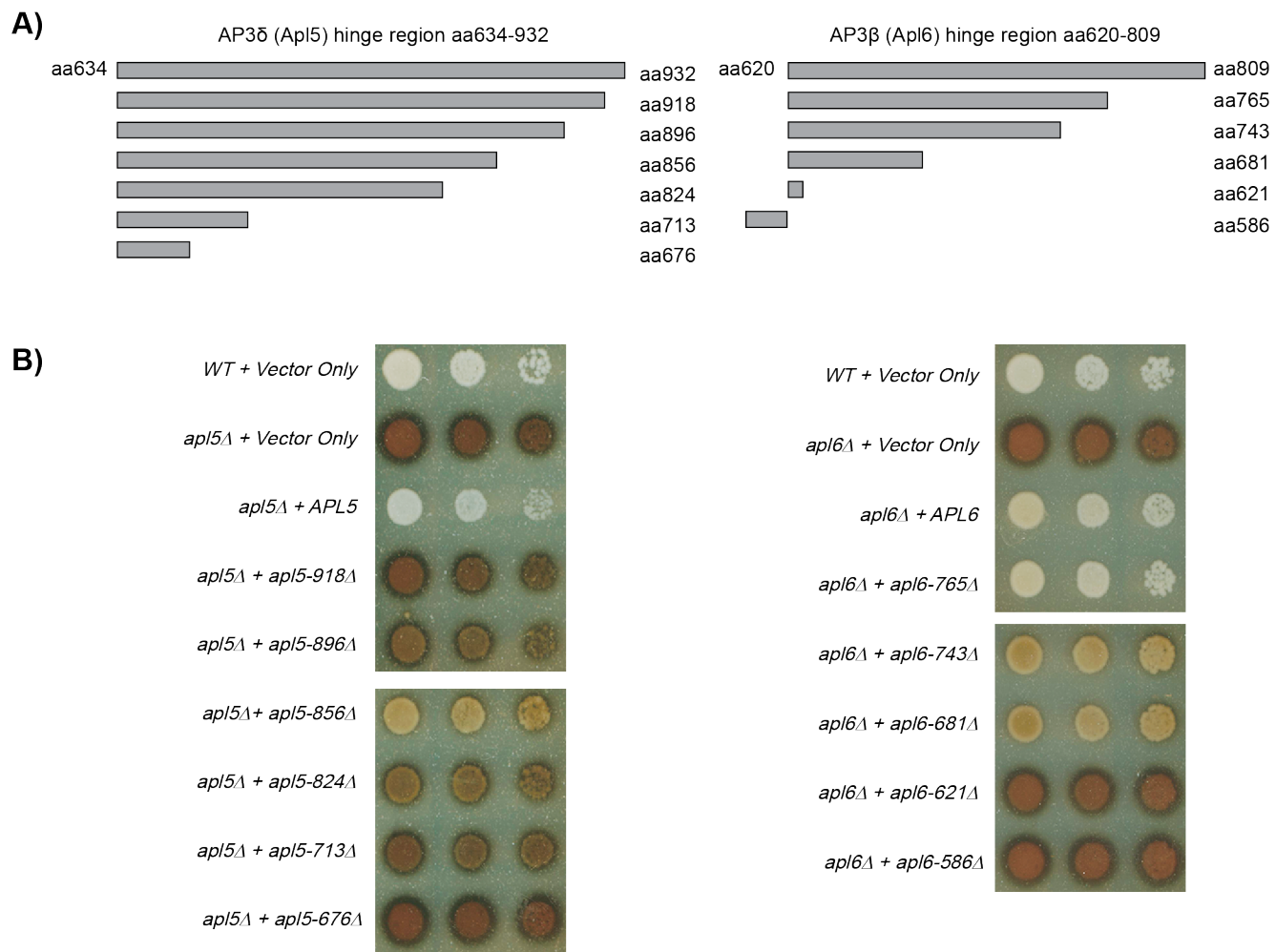


Fig. S2. AP-3 trafficking in yeast requires the hinge of each AP-3 large subunit. A) Diagrams depict the amount of C-terminal hinge region (grey boxes) in each of the *apl5* and *apl6* truncation-mutant alleles that were analyzed in (B) by overlay reaction to detect GNSS missorting to the plasma membrane. Full-length Apl5 is 932 amino acids; full-length Apl6 is 809 amino acids. B) Overlay reaction (see Materials and Methods) of agar medium spotted with a dilution series of wild-type cells versus *apl5 Δ* or *apl6 Δ* cells transformed with low-copy plasmids encoding the indicated *apl5* or *apl6* truncation-mutant alleles. Each overlay reaction was conducted for 30 minutes before imaging the plate. Cellular concentrations for each strain were 1.0, 0.1, and 0.01 OD₆₀₀ units/mL (left to right). The relatively weak GNSS missorting phenotype caused by the longer *apl5-856 Δ* truncation in comparison to shorter truncations (*apl5-918 Δ* and *apl5-896 Δ*) might signify a structural distortion that impacts Apl5 function when intermediate lengths of the hinge region are present, though such a possibility would require further analysis. Note that the relative amount of GNSS by *apl5-713 Δ* cells, which is qualitatively detected by overlay in Supplemental Figure 2B, is consistent with the fraction (80%) of GNSS missorted by *apl5-710 Δ* cells, which was measured quantitatively in Figure 2B. The *apl5-710 Δ* allele was used for all other experiments in this study because our prior results showed that the region of the hinge deleted by the *apl5-710 Δ* truncation (amino acids 711-932) directly binds Vps41, a subunit of the HOPS complex that tethers AP-3-coated vesicles to the vacuole (Angers and Merz, 2009).

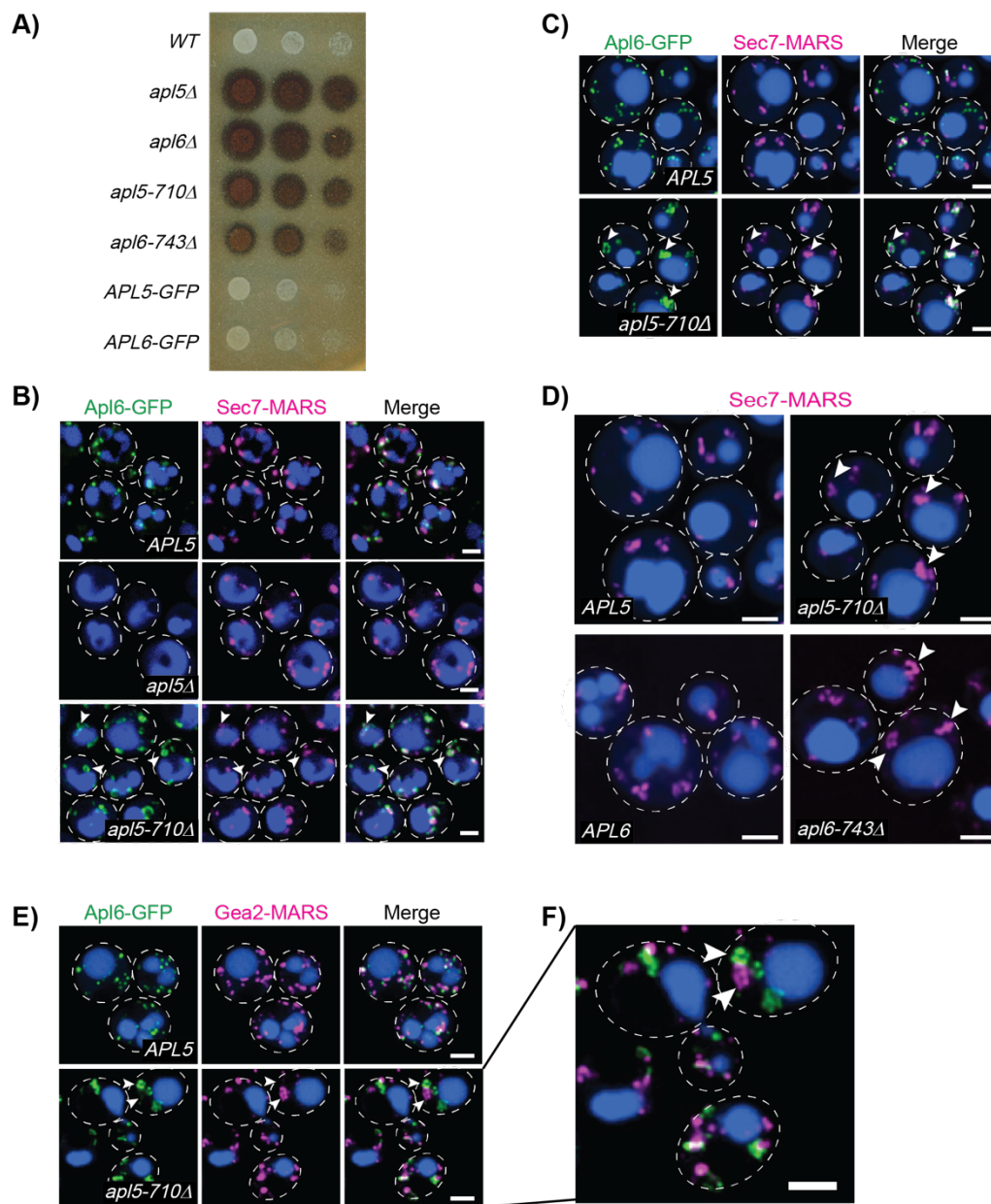


Fig. S3. Truncation of either hinge region causes AP-3 accumulation at the Golgi. All scale bars are 2 μm. A) GNSS overlay of strains expressing Apl5 or Apl6 truncation mutants or expressing GFP-tagged Apl5 or Apl6. Overlay reaction was allowed to continue for 30 minutes before imaging the plate. Cellular concentration for each strain was 1, 0.1, and 0.001 OD₆₀₀ units/mL (left to right). B) Images showing AP-3 localization relative to Sec7. AP-3 subunits tagged with GFP were expressed at their endogenous loci. Sec7-MARS was expressed from the pRS415 plasmid. The vacuole lumen was stained with CMAC Blue. C) Super-resolution confocal fluorescence microscopy showing distribution of AP-3 relative to Sec7. Arrowheads indicate rounded structures for both Sec7 and AP-3. D) Zoomed in image of Sec7 showing abnormal structure in AP-3 hinge truncation mutants. Arrowheads indicate round structures. E) Super-resolution confocal fluorescence microscopy showing distribution of Apl6-GFP relative to Gea2-Mars. Arrowheads indicate rounded structures for both Gea2-Mars and Apl6-GFP. F) Zoomed in image of Gea2 and AP-3 round structures in AP-3 truncation mutants.

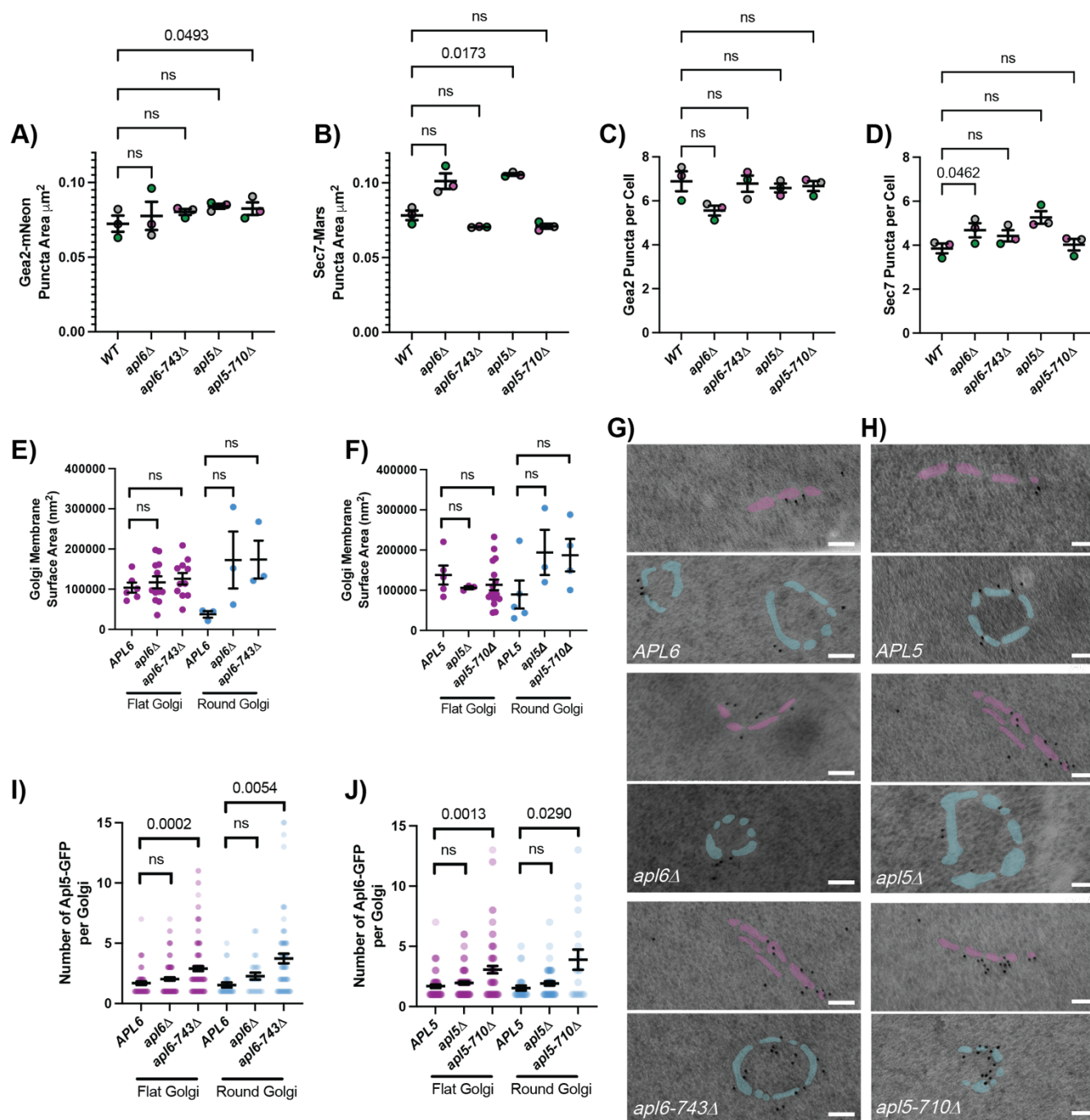


Fig. S4. AP-3 dysfunction alters Golgi morphology. A-B) Quantitation of average puncta size by area in square microns of Gea2-mNeon (A) and Sec7-Mars (B). Each point represents the averages of at least 200 cells. Error bars show SEM. P-values were determined by Dunett's test. C-D) Quantitation of average count of puncta per cell of Gea2-mNeon (C) and Sec7-Mars (D). Each point represents the averages of at least 200 cells. Error bars show SEM. P-values were determined by Dunett's test. E-F) Quantitation of the average membrane surface areas of flat and round Golgi in *apl6* mutant cells (E) and *apl5* mutant cells (F). Error bars show SEM. Magenta bars represent flat Golgi data; teal bars represent round Golgi data. P-values were determined using Dunnett's test. G-H) Immuno-gold labeling of APL5-GFP (G) and APL6-GFP (H) in wild-type and mutant AP-3 strains. Upper panels show flat Golgi in magenta while lower panels show round Golgi in cyan. Scale bars indicate 100 nm. I-J) Quantitation of the number of gold particles observed by immuno-EM using anti-GFP antibodies. Error bars show SEM. Magenta bars represent flat Golgi data, teal bars represent round Golgi data. P-values were determined using Dunnett's test.

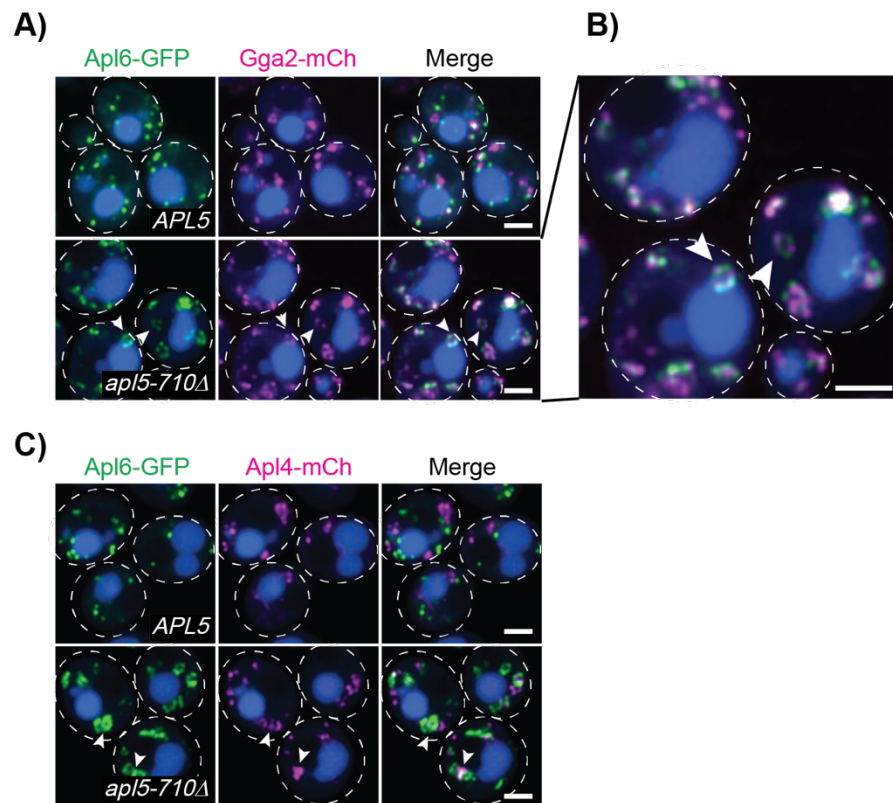


Fig. S5. Budding deficiency causes AP-3 to accumulate onto late Golgi adaptors. All scale bars are 2 μ m.

A) Super-resolution confocal fluorescence microscopy showing the distribution of AP-3 relative to Gga2. The vacuole lumen was stained with CMAC Blue and cell outlines are shown with white dotted lines. Arrowheads indicate rounded structures for both Gga2 and AP-3. B) Zoomed in image of AP-3 and GGA commingling donuts. C) Super-resolution confocal fluorescence microscopy showing distribution of AP-3 relative to AP-1. AP-3 subunits tagged with GFP and Apl4 tagged with mCherry were expressed at their endogenous loci. The vacuole lumen was stained with CMAC Blue and cell outlines are shown with white dotted lines. Arrowheads indicate rounded structures for both AP-1 and AP-3.

Table S1. Yeast strains used in this study

Strain Name	Genotype	Reference
BY4742	<i>MATa his3Δ1 leu2Δ0 lys2Δ0 ura3Δ0</i>	ATCC
GPY1100	<i>MATalpha leu2-3,112 ura3-52 his4-519 trpl can1</i>	Payne and Schekman, 1989
GOY844	GPY1100; <i>apl2Δ::KANMX6</i>	This Study
GOY822	GPY1100; <i>apl5Δ::KANMX6</i>	This Study
GOY863	GPY1100; <i>apl5-710Δ::KANMX6</i>	This Study
GOY891	GPY1100; <i>apl6Δ::KANMX6</i>	This Study
GOY861	GPY1100; <i>apl6-743Δ::KanMX6</i>	This Study
GPY418	<i>MATalpha leu2-3,112 ura3-52 his4-519 trpl can1; chc1-521</i>	Tan et al., 1993
GOY845	GPY418; <i>apl2Δ::KANMX6</i>	This Study
GOY823	GPY418; <i>apl5Δ::KANMX6</i>	This Study
GOY864	GPY418; <i>apl5-710Δ::KANMX6</i>	This Study
GOY894	GPY418; <i>apl6Δ::KANMX6</i>	This Study
GOY862	GPY418; <i>apl6-743Δ::KANMX6</i>	This Study
JTY01	BY4741; <i>suc2ΔGNSS::NATMX</i>	This Study
GOY696	BY4741; <i>suc2ΔGNSS::NATMX; apl5Δ::HIS3MX6</i>	This Study
GOY697	BY4741; <i>suc2ΔGNSS::NATMX; apl5-710Δ::HIS3MX6</i>	This Study
LDY49	BY4741; <i>suc2ΔGNSS::NATMX; apl6Δ::HIS3MX6</i>	This Study
GOY741	BY4741; <i>suc2ΔGNSS::NATMX; apl6-743Δ::HIS3MX6</i>	This Study
GOY788	BY4742; <i>vam3Δ::KANMX6; suc2Δ::HIS3MX6</i>	This Study
GOY760	SEY6210; <i>Apl5-iGFPx6::URA3</i>	This Study
GOY761	SEY6210; <i>Apl5-iGFPx6::URA3; apl6Δ::HIS3MX6</i>	This Study
GOY763	SEY6210; <i>Apl5-iGFPx6::URA3; apl6-743Δ::HIS3MX6</i>	This Study
GOY699	SEY6210; <i>Apl6-msGFPx3::URA3</i>	This Study
GOY702	SEY6210; <i>Apl6-msGFPx3::URA3; apl5Δ::HIS3MX6</i>	This Study
GOY703	SEY6210; <i>Apl6-msGFPx3::URA3; apl5-710Δ::HIS3MX6</i>	This Study

CFY2401	SEY6210a; <i>Gea2-3xMars::TRP1</i>	Highland and Fromme, 2021
MJLY129	SEY6210a; <i>Gea2-3xMars::TRP1; Apl5-iGFPx6::URA3</i>	This Study
MJLY122	SEY6210a; <i>Gea2-3xMars::TRP1; Apl5-iGFPx6::URA3; apl6-743Δ::HIS3MX6</i>	This Study
MJLY118	SEY6210a; <i>Gea2-3xMars::TRP1; Apl6-msGFPx3::URA3</i>	This Study
MJLY120	SEY6210a; <i>Gea2-3xMars::TRP1; Apl6-msGFPx3::URA3; apl5-710Δ::HIS3MX6</i>	This Study
CFY2378	SEY6210a; <i>Gea2-mNeon::HIS3; Sec7-Mars::TRP1</i>	Gustafson and Fromme, 2017
MJLY126	SEY6210a; <i>Gea2-mNeon::HIS3; Sec7-Mars::TRP1; apl5Δ::KANMX6</i>	This Study
MJLY107	SEY6210a; <i>Gea2-mNeon::HIS3; Sec7-Mars::TRP1; apl5-710Δ::KANMX6</i>	This Study
MJLY127	SEY6210a; <i>Gea2-mNeon::HIS3; Sec7-Mars::TRP1; apl6Δ::KANMX6</i>	This Study
MJLY108	SEY6210a; <i>Gea2-mNeon::HIS3; Sec7-Mars::TRP1; apl6-743Δ::KANMX6</i>	This Study
GOY875	SEY6210; <i>Apl5-iGFPx6::URA3; Gga2-mCherry::hphMX6</i>	This Study
GOY851	SEY6210; <i>Apl5-iGFPx6::URA3; Gga2-mCherry::hphMX6; apl6-743Δ::HIS3MX6</i>	This Study
GOY880	SEY6210; <i>Apl6-msGFPx3::URA3; Gga2-mCherry::hphMX6</i>	This Study
GOY881	SEY6210; <i>Apl6-msGFPx3::URA3; Gga2-mCherry::hphMX6; apl5-710Δ::HIS3MX6</i>	This Study
GOY819	SEY6210; <i>Apl5-iGFPx6::URA3; Apl4-mCherry::hphMX6</i>	This Study
GOY821	SEY6210; <i>Apl5-iGFPx6::URA3; Apl4-mCherry::hphMX6; apl6-743Δ::HIS3MX6</i>	This Study
GOY878	SEY6210; <i>Apl6-msGFPx3::URA3; Apl4-mCherry::hphMX6</i>	This Study
GOY879	SEY6210; <i>Apl6-msGFPx3::URA3; Apl4-mCherry::hphMX6; apl5-710Δ::HIS3MX6</i>	This Study
SEY6210	<i>MATa leu2-3,112 ura3-52 his3Δ200 trp1-Δ901 lys2-Δ801 suc2-Δ9</i>	Robinson et al., 1988
GOY4	SEY6210; <i>apl5Δ::HIS3</i>	Cowles et al., 1997
apl6Δ	SEY6210; <i>apl6Δ::HIS3</i>	Cowles et al., 1997
GOY700	SEY6210; <i>apl5-710Δ::HIS3MX6</i>	This Study
GOY627	SEY6210; <i>apl6-743Δ::HIS3MX6</i>	This Study
GPY2151	SEY6210; <i>gga1Δ::HIS3</i>	Costaguta et al., 2001
GPY2149	SEY6210; <i>gga2Δ::HIS3</i>	Costaguta et al., 2001
GPY3431	SEY6210; <i>gga1Δ::HIS3; gga2Δ::HIS3</i>	Costaguta et al., 2006
AMY2460	SEY6210; <i>Apl5-ttx-GFP::TRP1; apl6Δ::KANMX4</i>	This Study

Table S2. Plasmids used in this study

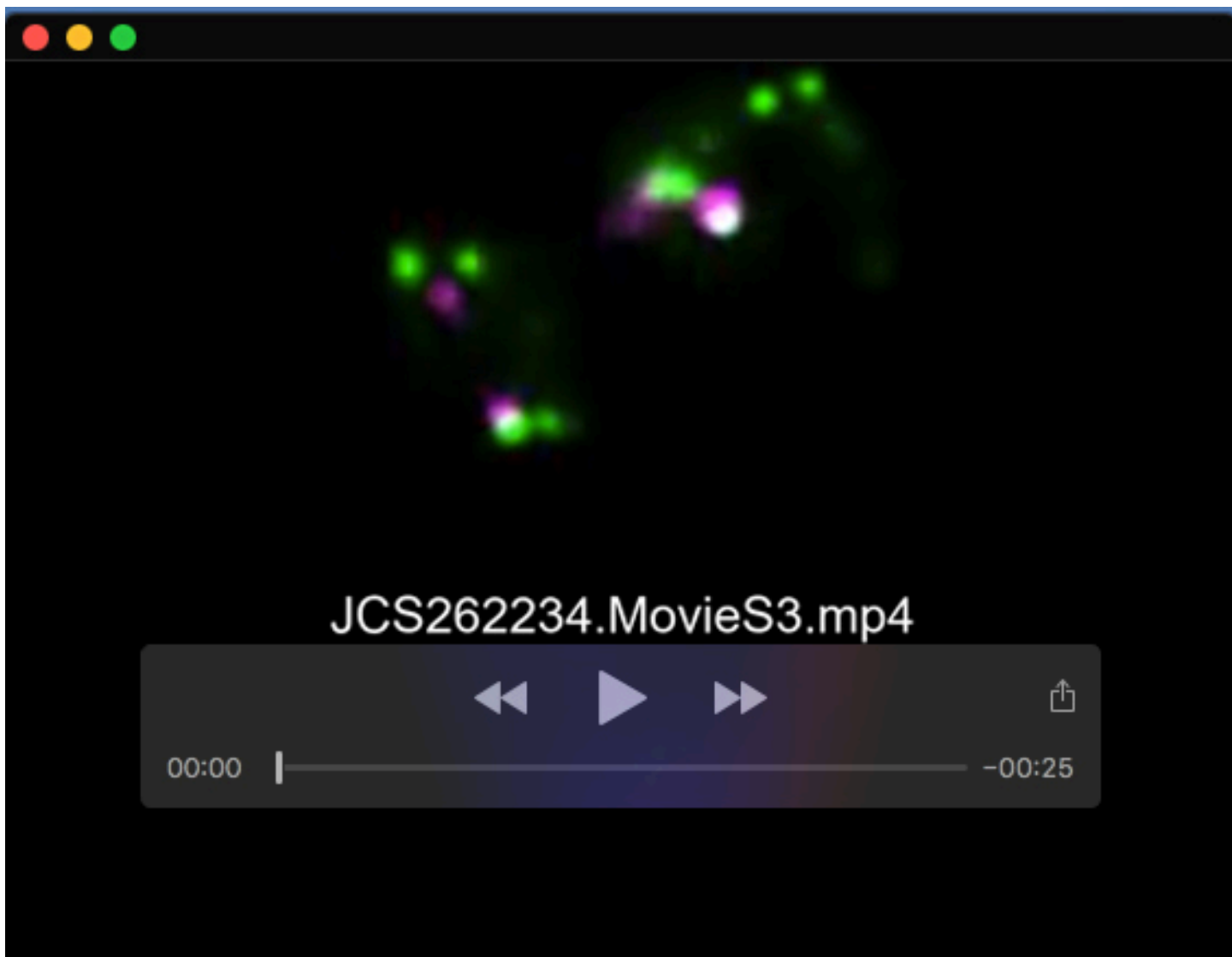
Plasmid Name	Genotype	Reference
AMB501	<i>GST-APL4</i> ⁷¹⁷⁻⁸³²	Angers and Merz, 2009
AMB508	<i>GST-APL4</i> ⁶²²⁻⁸³²	This Study
AMB436	<i>GST-APL5</i> ⁷¹¹⁻⁹³²	Angers and Merz, 2009
AMB499	<i>GST-APL5</i> ⁷¹¹⁻⁹³² <i>cbmΔ</i>	This Study
AMB504	<i>GST-APL5</i> ⁶¹⁵⁻⁹³²	This Study
AMB437	<i>GST-APL6</i> ⁶⁷³⁻⁸⁰⁹	Angers and Merz, 2009
AMB506	<i>GST-APL6</i> ⁶²⁵⁻⁸⁰⁹	This Study
pParallel-1-GST	<i>GST</i>	Sheffield et al., 1999
pLC1514	<i>GNSS; CEN URA3</i>	This Study
AMB1918	<i>APL5</i> ¹⁻⁹¹⁸ in <i>pRS416</i>	This Study
AMB1917	<i>APL5</i> ¹⁻⁸⁶⁹ in <i>pRS416</i>	This Study
AMB1916	<i>APL5</i> ¹⁻⁸⁵⁶ in <i>pRS416</i>	This Study
AMB1915	<i>APL5</i> ¹⁻⁸²⁴ in <i>pRS416</i>	This Study
AMB1914	<i>APL5</i> ¹⁻⁷¹³ in <i>pRS416</i>	This Study
AMB1913	<i>APL5</i> ¹⁻⁶⁷⁶ in <i>pRS416</i>	This Study
AMB1614	<i>APL5</i> in <i>pRS416</i>	This Study
AMB1602	<i>APL6</i> ¹⁻⁷⁶⁵ in <i>pRS416</i>	This Study
AMB1514	<i>APL6</i> ¹⁻⁷⁴³ in <i>pRS416</i>	This Study
AMB1601	<i>APL6</i> ¹⁻⁶⁸¹ in <i>pRS416</i>	This Study
AMB1600	<i>APL6</i> ¹⁻⁶²¹ in <i>pRS416</i>	This Study
AMB1599	<i>APL6</i> ¹⁻⁵⁸⁶ in <i>pRS416</i>	This Study
AMB743	<i>APL6</i> in <i>pRS416</i>	This Study
pLT45	<i>mRFPmars-Sec7</i> in <i>pRS415</i>	Thomas and Fromme, 2016
Ylplac211-Apl5-iGFPx6	<i>APL5-iGFPx6::URA3</i>	Day et al., 2018
Ylplac211-Apl6-msGFPx3	<i>APL6-msGFPx3::URA3</i>	Day et al., 2018
pFA6a-mChery-hphMX6	<i>mCherryx6::hphMX6</i>	Wang et al., 2014
pCYI50	<i>CPY-Inv; CEN URA3</i>	Johnson et al., 1987



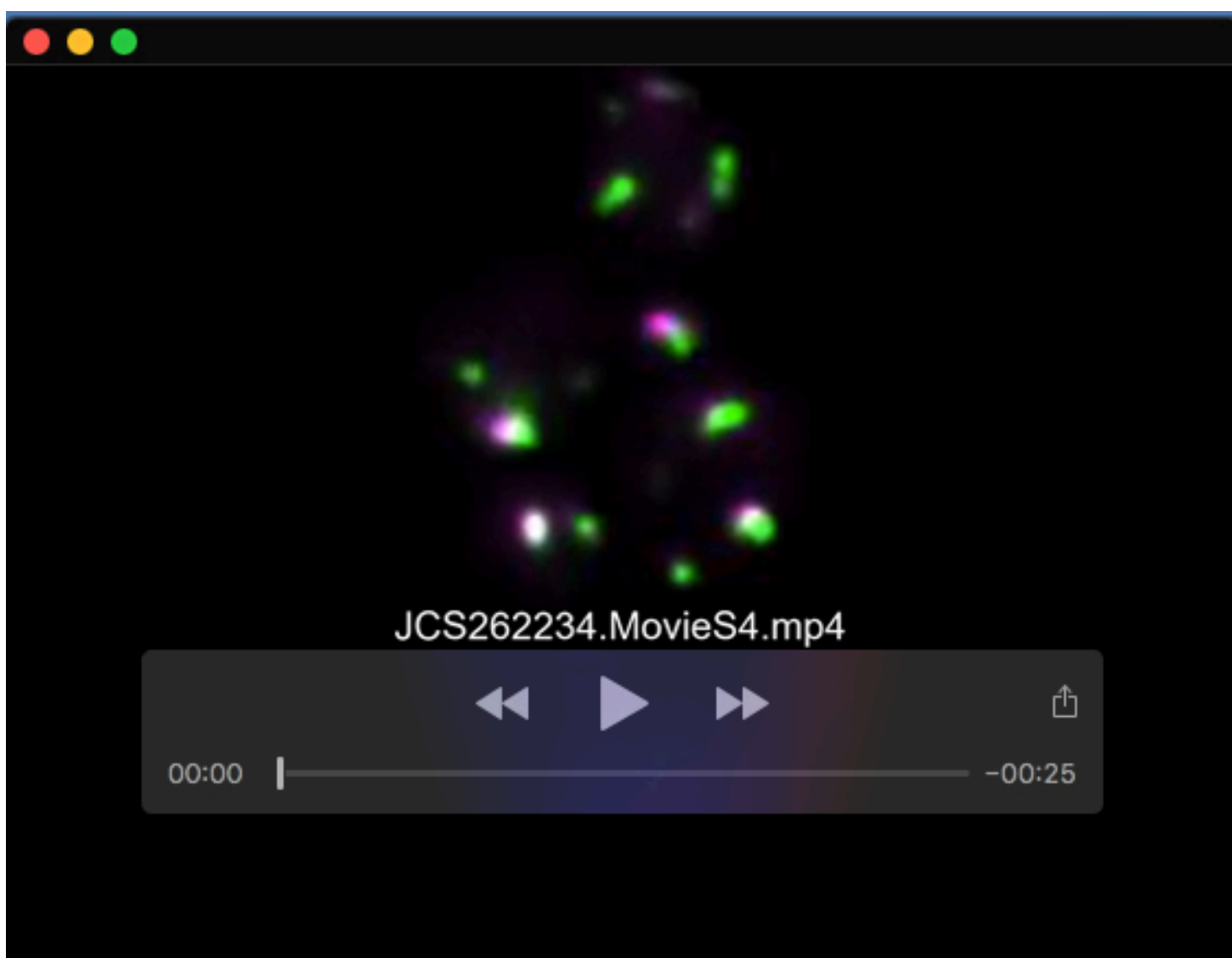
Movie 1. 30-second movie of wild-type *APL6* cells expressing Apl5-GFP and MARS-Sec7. Frames were taken at 50-ms intervals in a single plane.



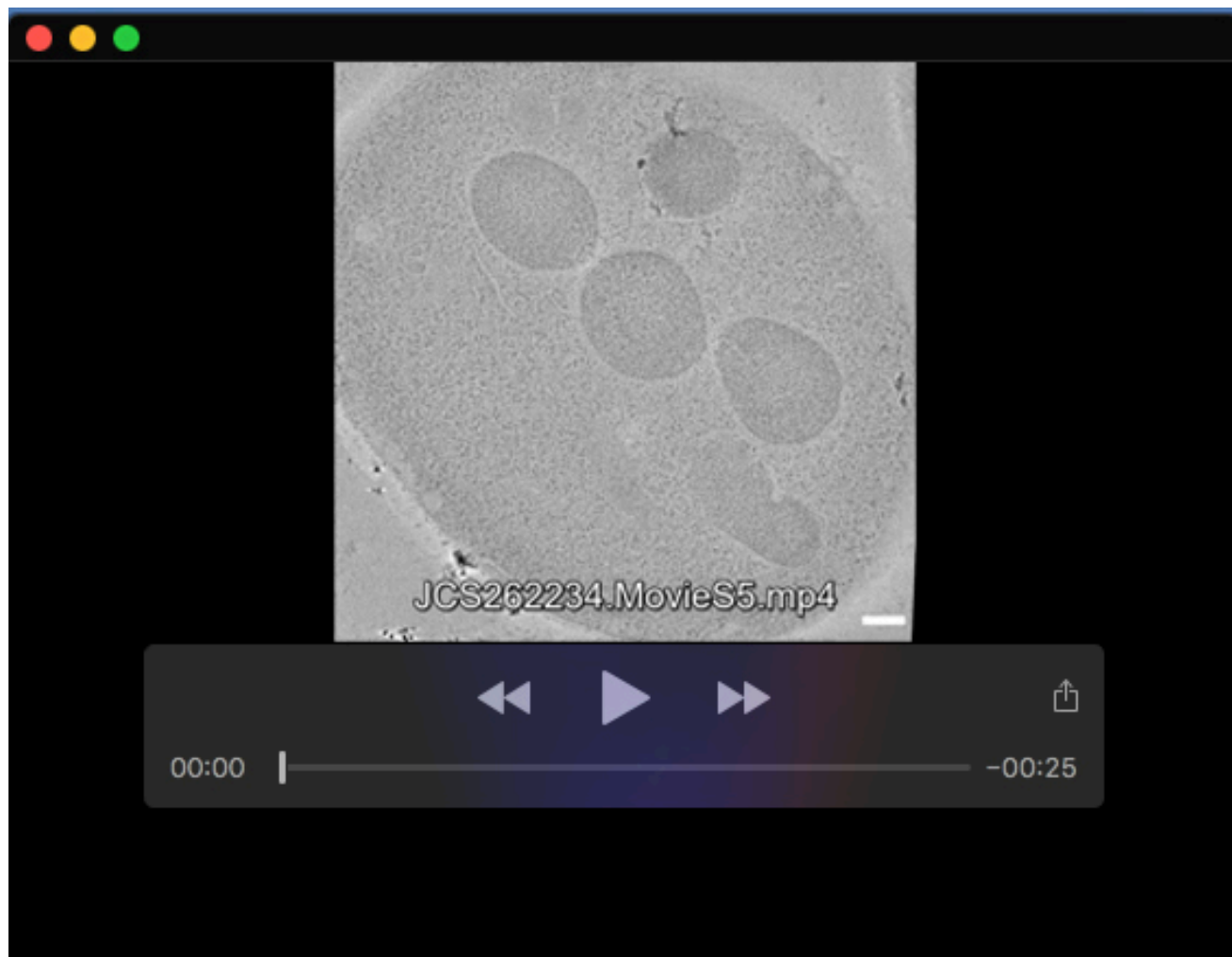
Movie 2. 30-second movie of *apl6-743Δ* cells expressing Apl5-GFP and MARS-Sec7. Frames were taken at 50-ms intervals in a single plane.



Movie 3. 30-second movie of wild-type *APL5* cells expressing Apl6-GFP and MARS-Sec7. Frames were taken at 50-ms intervals in a single plane.



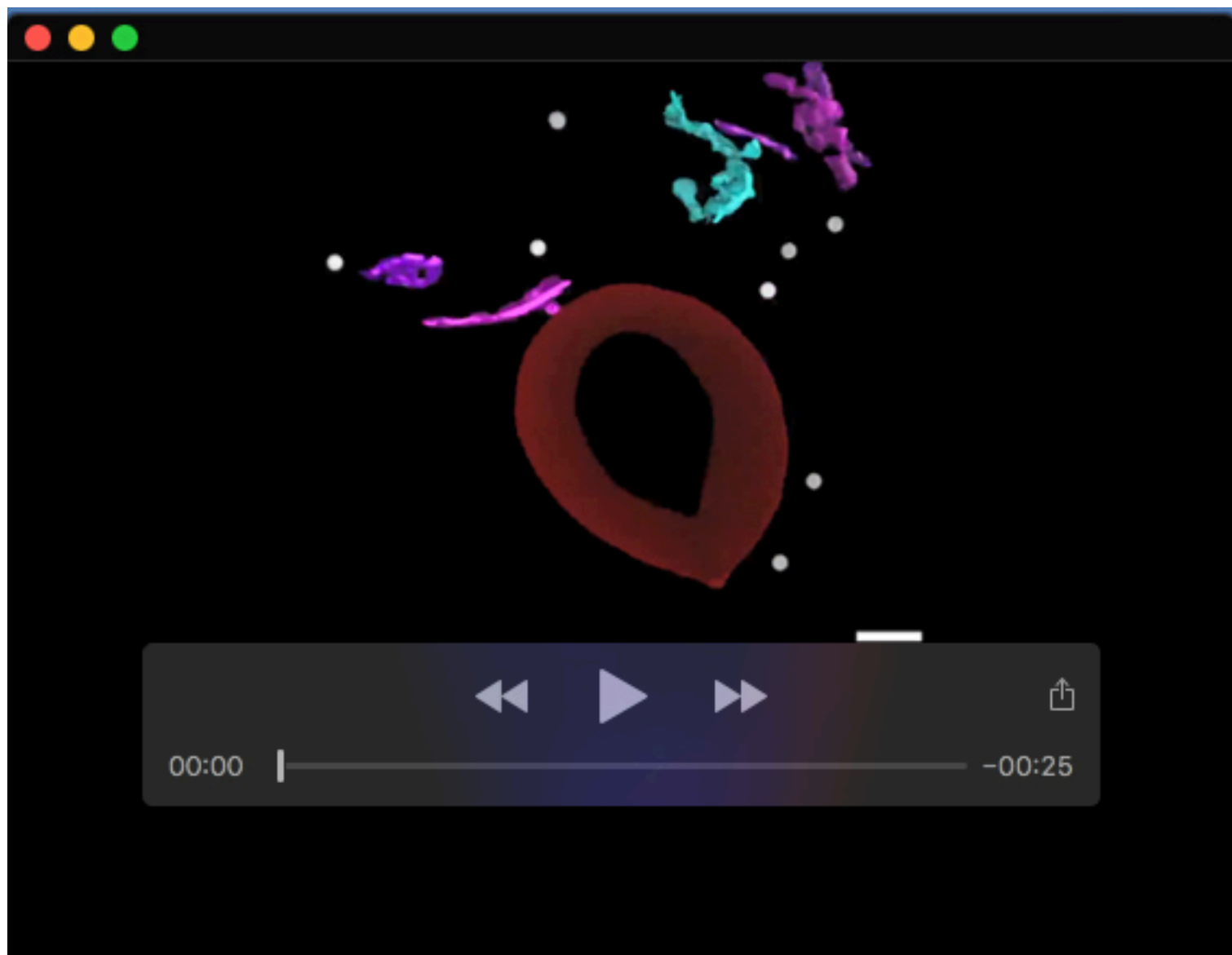
Movie 4. 30-second movie of wild-type *apl5-710Δ* cells expressing Apl6-GFP and MARS-Sec7. Frames were taken at 50-ms intervals in a single plane.



Movie 5. EM tomography data showing 3-D renderings of Golgi, vacuoles, and vesicles in *APL6* cells. Flat Golgi shown in magenta, round Golgi shown in cyan, curved Golgi shown in purple, vacuole membrane shown in red, and cytosolic vesicles shown in grey. Scale bars show 200 nm when zoomed out (beginning) and 100 nm when zoomed in (end).



Movie 6. EM tomography data showing 3-D renderings of Golgi, vacuoles, and vesicles in *apl6Δ* cells. Flat Golgi shown in magenta, round Golgi shown in cyan, curved Golgi shown in purple, vacuole membrane shown in red, and cytosolic vesicles shown in grey. Scale bars show 200 nm when zoomed out (beginning) and 100 nm when zoomed in (end).



Movie 7. EM tomography data showing 3-D renderings of Golgi, vacuoles, and vesicles in *apl6-743Δ* cells. Flat Golgi shown in magenta, round Golgi shown in cyan, curved Golgi shown in purple, vacuole membrane shown in red, and cytosolic vesicles shown in grey. Scale bars show 200 nm when zoomed out (beginning) and 100 nm when zoomed in (end).